

Eye of Horus: A Vision-based Framework for Real-time Water Level Measurement

Seyed Mohammad Hassan Erfani¹, Corinne Smith¹, Zhenyao Wu¹, Elyas Asadi Shamsabadi², Farboud Khatami¹, Austin R.J. Downey¹, Jasim Imran¹, and Erfan Goharian¹

¹University of South Carolina

²University of Sydney

March 9, 2023

Abstract

Heavy rains and tropical storms often result in floods, which are expected to increase in frequency and intensity. Flood prediction models and inundation mapping tools provide decision-makers and emergency responders with crucial information to better prepare for these events. However, the performance of models relies on the accuracy and timeliness of data received from in-situ gaging stations and remote sensing; each of these data sources has its limitations, especially when it comes to real-time monitoring of floods. This study presents a vision-based framework for measuring water levels and detecting floods using Computer Vision and Deep Learning (DL) techniques. The DL models use time-lapse images captured by surveillance cameras during storm events for the semantic segmentation of water extent in images. Three different DL-based approaches, namely PSPNet, TransUNet, and SegFormer, were applied and evaluated for semantic segmentation. The predicted masks are transformed into water level values by intersecting the extracted water edges, with the 2D representation of a point cloud generated by an Apple iPhone 13 Pro LiDAR sensor. The estimated water levels were compared to reference data collected by an ultrasonic sensor. The results showed that SegFormer outperformed other DL-based approaches by achieving 99.55% and 99.81% for Intersection over Union (IoU) and accuracy, respectively. Moreover, the highest correlations between reference data and the vision-based approach reached above 0.98 for both the coefficient of determination (R²) and Nash-Sutcliffe Efficiency. This study demonstrates the potential of using surveillance cameras and Artificial Intelligence for hydrologic monitoring and their integration with existing surveillance infrastructure.

EYE OF HORUS: A VISION-BASED FRAMEWORK FOR REAL-TIME WATER LEVEL MEASUREMENT

Mohammad H. Erfani¹, Corinne Smith², Zhenyao Wu³, Elyas Asadi Shamsabadi⁴,
Farboud Khatami¹, Austin R.J. Downey^{1,2}, Jasim Imran¹, and Erfan Goharian^{*1}

¹Department of Civil & Environmental Engineering, University of South Carolina Columbia, SC 29208, USA

²Department of Mechanical Engineering, University of South Carolina, Columbia, SC 29208, USA

³Department of Computer Science & Engineering, University of South Carolina, Columbia, SC 29201, USA

⁴School of Civil Engineering, Faculty of Engineering, The University of Sydney, Sydney, NSW 2006, Australia

Abstract

Heavy rains and tropical storms often result in floods, which are expected to increase in frequency and intensity. Flood prediction models and inundation mapping tools provide decision-makers and emergency responders with crucial information to better prepare for these events. However, the performance of models relies on the accuracy and timeliness of data received from in-situ gaging stations and remote sensing; each of these data sources has its limitations, especially when it comes to real-time monitoring of floods. This study presents a vision-based framework for measuring water levels and detecting floods using Computer Vision and Deep Learning (DL) techniques. The DL models use time-lapse images captured by surveillance cameras during storm events for the semantic segmentation of water extent in images. Three different DL-based approaches, namely PSPNet, TransUNet, and SegFormer, were applied and evaluated for semantic segmentation. The predicted masks are transformed into water level values by intersecting the extracted water edges, with the 2D representation of a point cloud generated by an Apple iPhone 13 Pro LiDAR sensor. The estimated water levels were compared to reference data collected by an ultrasonic sensor. The results showed that SegFormer outperformed other DL-based approaches by achieving 99.55% and 99.81% for Intersection over Union (IoU) and accuracy, respectively. Moreover, the highest correlations between reference data and the vision-based approach reached above 0.98 for both the coefficient of determination (R^2) and Nash-Sutcliffe Efficiency. This study demonstrates the potential of using surveillance cameras and Artificial Intelligence for hydrologic monitoring and their integration with existing surveillance infrastructure.

1 Introduction

Flood forecasts and Flood Inundation Mapping (FIM) can play an important role in saving human lives and reducing damages by providing timely information for evacuation planning, emergency management, and relief efforts [Gebrehiwot et al., 2019]. These models and tools are designed to identify and predict inundation areas and the severity of damage caused by storm events. Two primary sources of data for these models are in-situ gaging networks and remote sensing. For example, in-situ stream gages, such as those operated by the United States Geological Survey (USGS) provide useful stream-flow information like water height and discharge at monitoring sites [Turnipseed and Sauer, 2010]. However, they cannot provide an adequate spatial resolution of streamflow characteristics [Lo et al., 2015]. The limitation of in-situ stream gages is further exacerbated by the lack of systematic installation along the waterways and accessibility issues [Li et al., 2018; King et al., 2018]. Satellite data and remote sensing can complement in-situ gage data by providing information at a larger spatial scale [Alsdorf et al., 2007]. However, continuous monitoring data for a region of interest remains to be a problem due to the limited revisit intervals of satellites, cloud cover, and systematic departures or biases [Panteras and Cervone, 2018]. Crowdsourcing methods have gained attention as a potential solution but their reliability is questionable [Schnebele et al., 2014; Goodchild, 2007; Howe, 2008]. To address these limitations and enhance real-time monitoring capabilities, surveillance cameras are inves-

*goharian@cec.sc.edu

46 tigated here as a new source of data for hydrologic monitoring and flood data collection. However, this
47 requires a significant investment in Computer Vision (CV) and Artificial Intelligence (AI) techniques
48 to develop reliable methods for detecting water in surveillance images and translating that information
49 into numerical data.

50 Recent advances in CV offer new techniques for processing image data for the quantitative measure-
51 ments of physical attributes from a site [Forsyth and Ponce, 2002]. However, there is limited knowledge
52 of how visual information can be used to estimate physical water parameters using CV techniques.
53 Inspired by the principle of the float method, Tsubaki et al. [2011] used different image processing tech-
54 niques to analyze images captured by closed-circuit television (CCTV) systems installed for surveillance
55 purposes to measure the flow rate during flood events. In another example, Kim et al. [2011] proposed
56 a method for measuring water level by detecting the borderline between a staff gauge and the surface
57 of water based on image processing of the captured image of the staff gage installed in the middle of
58 the river. As the use of images for environmental monitoring becomes more popular, several studies
59 have investigated the source and magnitude of errors common in image-based measurement systems,
60 such as the effect of image resolution, lighting effects, perspective, lens distortion, water meniscus,
61 and temperature changes [Elias et al., 2020; Gilmore et al., 2013]. Furthermore, proposed solutions
62 to resolve difficulties originating from poor visibility have been developed to better identify readings
63 on staff gages [Zhang et al., 2019]. Recently, Deep Learning (DL) has become prevalent across a wide
64 range of disciplines, particularly in applied sciences such as CV and engineering.

65 DL-based models have been utilized by the water resources community to determine the extent of water
66 and waterbodies visible in images captured by surveillance camera systems. These models can estimate
67 the water level [Pally and Samadi, 2022]. In a similar vein, Moy de Vitry et al. [2019] employed a DL-
68 based approach to identify floodwater in surveillance footage and introduced a novel qualitative flood
69 index, SOFI, to determine water level fluctuations. SOFI was calculated by taking the aspect ratio of
70 the area of the water surface detected within an image to the total area of the image. However, these
71 types of methods, which make prior assumptions and estimate water level fluctuation roughly, cannot
72 serve as a vision-based alternative for measuring streamflow characteristics. More systematic studies
73 adopted photogrammetry to reconstruct a high-quality 3D model of the environment with a high
74 spatial resolution to have a precise estimation of real-world coordination while measuring streamflow
75 rate and stage. For example, Eltner et al. [2018, 2021] introduced a method based on Structure
76 from Motion (SfM), and photogrammetric techniques, to automatically measure the water stage using
77 low-cost camera setups.

78 Advances in photogrammetry techniques enable 3D surface reconstruction with a high temporal and
79 spatial resolution. These techniques are adopted to build 3D surface models from RGB imagery [West-
80 oby et al., 2012; Eltner and Schneider, 2015; Eltner et al., 2016]. However, most of the photogrammetric
81 methods are still expensive as they rely on differential global navigation satellite systems (DGNS),
82 ground control points (GCPs), commercial software, and data processing on an external computing
83 device [Froideval et al., 2019]. A LiDAR scanner, on the other hand, is now easily available since the
84 introduction of the iPad Pro and iPhone 12 Pro in 2020 by Apple. This device is the first smartphone
85 equipped with a native LiDAR scanner and offers a potential paradigm shift in digital field data acqui-
86 sition which puts these devices at the forefront of smartphone-assisted fieldwork [Tavani et al., 2022].
87 So far, the iPhone LiDAR sensor has been used in different studies such as forest inventories [Gollob
88 et al., 2021] and coastal cliff site [Luetzenburg et al., 2021]. The availability of LiDAR sensors to build
89 3D environments, and advancements in DL-based models offer a great potential to produce numerical
90 information from ground-based imageries.

91 This paper presents a vision-based framework for measuring water levels from time-lapse images. The
92 proposed framework introduces a novel approach by utilizing the iPhone LiDAR sensor as a laser scan-
93 ner, which is commonly available on consumer-grade devices, for scanning and constructing a 3D point
94 cloud of the region of interest. During the data collection phase, time-lapse images and ground truth
95 water level values were collected using an embedded camera and ultrasonic sensor. The water extent
96 in the captured images was determined automatically using semantic segmentation DL-based models.
97 For the first time, the performance of three different state-of-the-art DL-based approaches, including
98 Convolutional Neural Networks (CNN), hybrid CNN-Transformer, and Transformers-Multilayer Per-
99 ceptron (MLP), was evaluated and compared. CV techniques were applied for camera calibration, pose

100 estimation of the camera setup in each deployment, and 3D-2D reprojection of the point cloud onto
101 the image plane. Finally, K-Nearest Neighbors (KNN) was used to find the nearest projected (2D)
102 point cloud coordinates to the water line on the river banks, for estimating the water level in each
103 time-lapse image.

104 2 Deep Learning Architectures

105 Since this study tends to cover a wide range of DL approaches, this section solely focuses on reviewing
106 different DL-based architectures. So far, different DL networks were applied and evaluated for semantic
107 segmentation of the waterbodies within the RGB images captured by cameras [Erfani et al., 2022]. All
108 existing semantic segmentation approaches—CNN and Transformer-based—share the same objective of
109 classifying each pixel of a given image but differ in the network design.

110 CNN-based models were designed to imitate the recognition system of primates [Shamsabadi et al.,
111 2022], while possessing different network designs such as low-resolution representations learning [Long
112 et al., 2015; Chen et al., 2017], high-resolution representations recovering [Badrinarayanan et al., 2015;
113 Noh et al., 2015; Lin et al., 2017], contextual aggregation schemes [Yuan and Wang, 2018; Zhao et al.,
114 2017; Yuan et al., 2020], feature fusion and refinement strategy [Lin et al., 2017; Huang et al., 2019;
115 Li et al., 2019; Zhu et al., 2019; Fu et al., 2019]. CNN-based models follow local to global features in
116 different layers of the forward pass, which used to be thought of as a general intuition of the human
117 recognition system. In this system, objects are recognized through the analysis of texture and shape-
118 based clues—local and global representations and their relationship in the entire field of view. Recent
119 research, however, shows significant differences exist between the visual behavioral system of humans
120 and CNN-based models [Geirhos et al., 2018b; Dodge and Karam, 2017; De Cesarei et al., 2021; Geirhos
121 et al., 2020, 2018a], and reveal higher sensitivity of the visual systems in humans to global features
122 rather than local ones [Zheng et al., 2018]. This fact drew attention to models that focus on the global
123 context in their architectures.

124 Developed by Dosovitskiy et al. [2020], Vision Transformer (ViT) was the first model that showed
125 promising results on a computer vision task (image classification) without using convolution operation
126 in its architecture. In fact, ViT adopts “Transformers,” as a self-attention mechanism, to improve
127 accuracy. “Transformer” was initially introduced for sequence-to-sequence tasks such as text trans-
128 lation [Vaswani et al., 2017]. However, as applying the self-attention mechanism on all image pixels
129 is computationally expensive, the Transformer-based models could not compete with the CNN-based
130 models until the introduction of ViT architecture which applies self-attention calculations on the low-
131 dimension embedding of small patches originating from splitting the input image, to extract global
132 contextual information. Successful performance of ViT on image classification inspired several subse-
133 quent works on Transformer-based models for different computer vision tasks [Liu et al., 2021].

134 In this study, three different DL-based approaches including CNN, hybrid CNN-Transformer, and
135 Transformers-Multilayer Perceptron (MLP) were trained and tested for semantic segmentation of wa-
136 ter. For these approaches, the selected models were PSPNet [Zhao et al., 2017], TransUNet [Chen
137 et al., 2021] and SegFormer [Xie et al., 2021], respectively. The performance of these models is evalu-
138 ated and compared using conventional metrics, including class-wise Intersection over Union (IoU) and
139 per-pixel accuracy (ACC).

140 3 Study Area

141 In order to evaluate the performance of the proposed framework for measuring the water levels in rivers
142 and channels, a time-lapse camera system has been deployed at Rocky Branch, South Carolina. This
143 creek is approximately 6.5 km long and collects stormwater from the University of South Carolina
144 campus and the City of Columbia. Rocky Branch is subjected to rapid changes in water flow and
145 discharges into the Congaree River [Morsy et al., 2016]. The observation site is located within the
146 University of South Carolina campus behind 300 Main Street. An Apple iPhone 13 Pro LiDAR sensor
147 was used to scan the region of interest (see Figure 1a). Although there is no official information about
148 the technology and hardware specifications, Gollob et al. [2021] reports the LiDAR module operates
149 at the 8XX nm wavelength and consists of an emitter (Vertical Cavity Surface-Emitting Laser with

150 Diffraction Optics Element, VCSEL DOE) and a receptor (Single Photon Avalanche Diode array-
151 based Near Infrared Complementary Metal Oxide Semiconductor image sensor, SPAD NIR CMOS)
152 based on direct-time-of-flight technology. Comparisons between the Apple LiDAR sensor and other
153 types of laser scanners including hand-held, industrial, and terrestrial have been conducted by several
154 recent studies [Mokroš et al., 2021; Vogt et al., 2021]. Gollob et al. [2021] tested and reported the
155 performance of a set of eight different scanning apps, and found three applications including 3D
156 Scanner App, Polycam and SiteScape suitable for actual practice tests. The objective of this study
157 is not the evaluation of the iPhone LiDAR sensor and app performance. Therefore, the 3D Scanner
158 App [LABS, 2022] was used with the following settings: confidence = high, range = 5.0 m, masking =
159 none, and resolution = 5 mm, for scanning and 3D reconstruction processing. The scanned 3D point
160 cloud is shown in Figure 1b.

161 As the LiDAR scanner settings were set at the highest level of accuracy and computational demand,
162 scanning the whole region of interest at the same time was not possible. So, the experimental region
163 was divided into several sub-regions and scanned in multi-step. In order to assemble the sub-region
164 LiDAR scans, several GCPs were considered in the study area. These GCPs were measured by a
165 total station (Topcon GM Series). Moreover, 13 Aruco markers were installed for estimating extrinsic
166 camera parameters in each setup deployment. Since it was not possible to accurately measure the real-
167 world coordination of Aruco markers by the LiDAR scanner, the coordinates of the top-left corner
168 of markers were also measured by the surveying total station. The 3D point cloud scanned for each
169 sub-region was transformed into the total station coordinate system, and the real-world coordinates of
170 ArUco markers were appended to the 3D point cloud for the following analyses.

171 4 Methodology

172 This study introduces the Eye of Horus, a vision-based framework for hydrologic monitoring and
173 real-time water level measurements in bodies of water. The proposed framework includes three main
174 components. The first step is designing two deployable setups for data collection. These setups consist
175 of a programmable time-lapse camera run by Raspberry Pi and an ultrasonic sensor run by Arduino.
176 After collecting data, the first phase (Module 1) involves configuring and training DL-based models
177 for semantic segmentation of water in the captured images. In the second phase (Module 2), CV
178 techniques for camera calibration, spatial resection, and calculating projection matrix are discussed.
179 Finally, in the third phase (Module 3), an ML-based model uses the information achieved by CV
180 models to find the relationships between real-world coordinates of water level in the captured images
181 (see Figure 2).

182 4.1 Data Acquisition

183 Two different single-board computers (SBC) were used in this study, Raspberry Pi (Zero W) for
184 capturing time-lapse images of a river scene, and Arduino (Nano 3.x) for measuring water level as the
185 ground truth data. These devices were designed to communicate with each other, i.e., to trigger the
186 other to start or stop recording. During capturing time-lapse images, the Pi camera device triggers the
187 ultrasonic sensor for measuring the corresponding water level. The camera device is equipped with the
188 Raspberry Pi Camera Module 2 which has a Sony IMX219 8-megapixel sensor. This sensor is able to
189 capture an image size of $4,256 \times 2,832$ pixels. However, in this study, the image resolution was set to
190 $1,920 \times 1,440$ pixels to balance image quality and computational cost in subsequent image processing
191 steps. This setup is also equipped with a 1200 mAh UPS lithium battery power module to provide
192 uninterrupted power to the Pi SBC (see Figure 3a).

193 The Arduino-based device records the water level. The design is based on an unmanned aerial ve-
194 hicle (UAV) deployable sensor created by Smith et al. [2022]. The nRF24L01+ single-chip 2.4 GHz
195 transceiver allows the Arduino and Raspberry Pi to communicate via radio frequency (RF). The chip
196 is housed in both packages and the channel, pipe addresses, data rate, and transceiver/receiver con-
197 figuration are all set in the software. The HC-SR04 ultrasonic sensor is mounted to the base of the
198 Arduino device and provides a contactless water level measurement. Two permanent magnets at the
199 top of the housing attach to a ferrous structure and allow the ultrasonic sensor to be suspended up to
200 14 feet over the surface of the water. The device also includes a microSD card module and DS3231

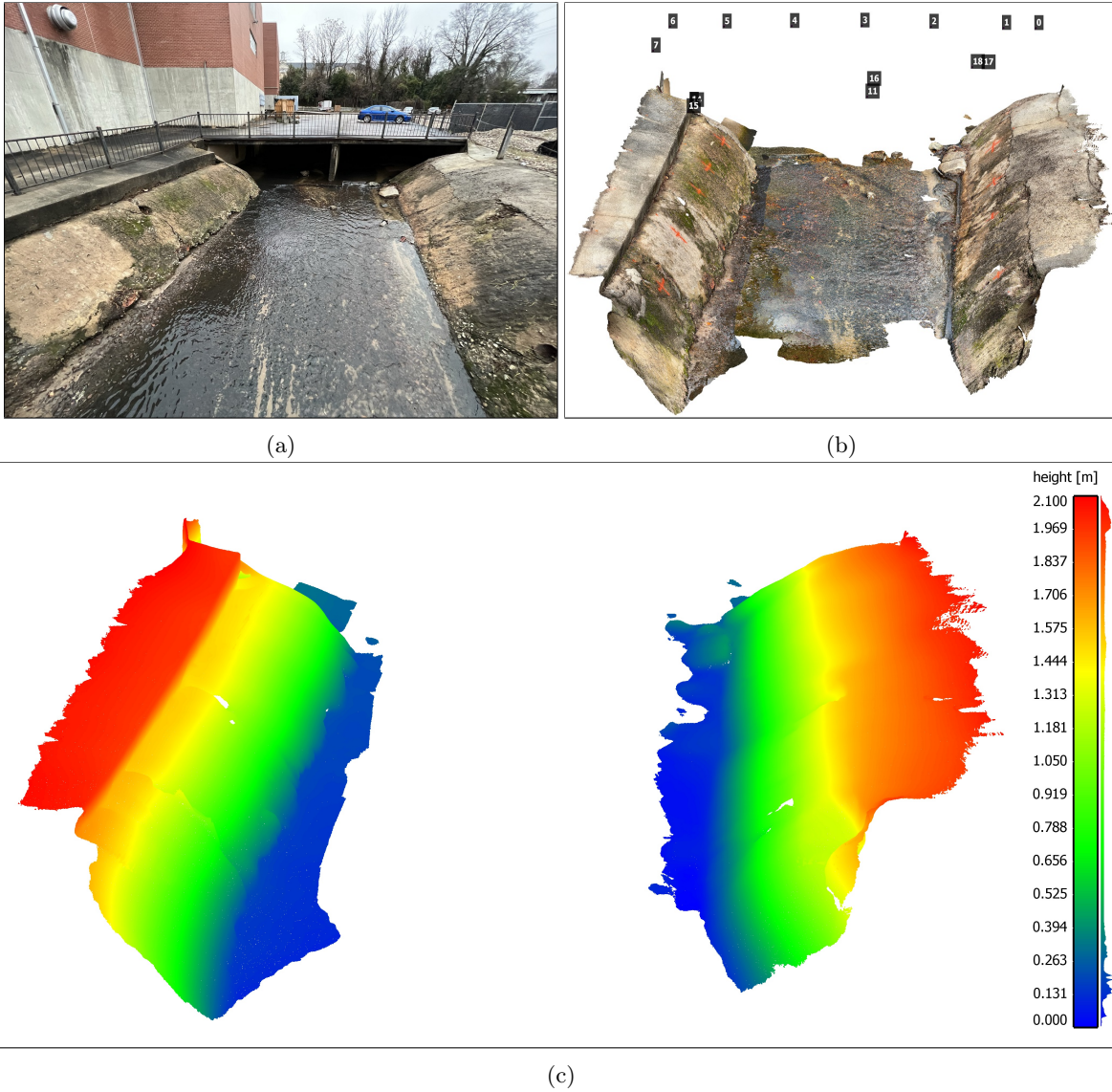


Figure 1: Study area of the Rocky Branch Creek. (a) View of the region of interest, (b) The scanned 3D point cloud of the region of interest including an indication of the ArUco markers' locations, and (c) The scalar field of left and right banks of Rocky Branch in the region of interest (the colorbar and the frequency distribution of z values for the captured points are shown on the right side).

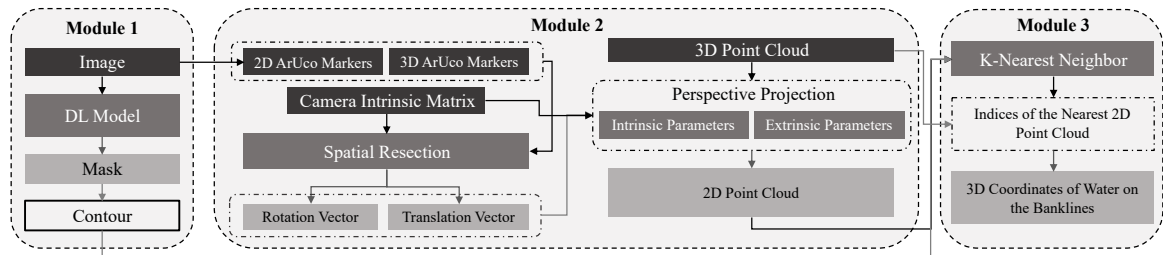


Figure 2: The Eye of Horus workflow includes three main modules starting from processing images captured by the time-lapse camera to estimating water level by projecting the waterline on river banks using CV techniques.

201 real-time clock, which enable data logging and storage on-device as well as transmission. The device
 202 is powered by a rechargeable 7.4V 1500 mAh lithium polymer battery (see Figure 3b).

203 The Arduino device waits to receive a ping from the Raspberry Pi device to initiate data collection.
 204 The ultrasonic sensor measures the distance from the sensor transducer to the surface of the water.
 205 The nRF24L01+ transmits this distance to the Raspberry Pi device and saves the measurement and a
 206 time stamp from the real-time clock to an onboard microSD card. This acts as backup data storage, in
 207 case transmission to the Raspberry Pi fails. The nRF24L01+ RF transceivers have an experimentally
 208 determined range of up to 30 ft which allows flexibility in the relative placement of the camera to the
 209 measuring site.

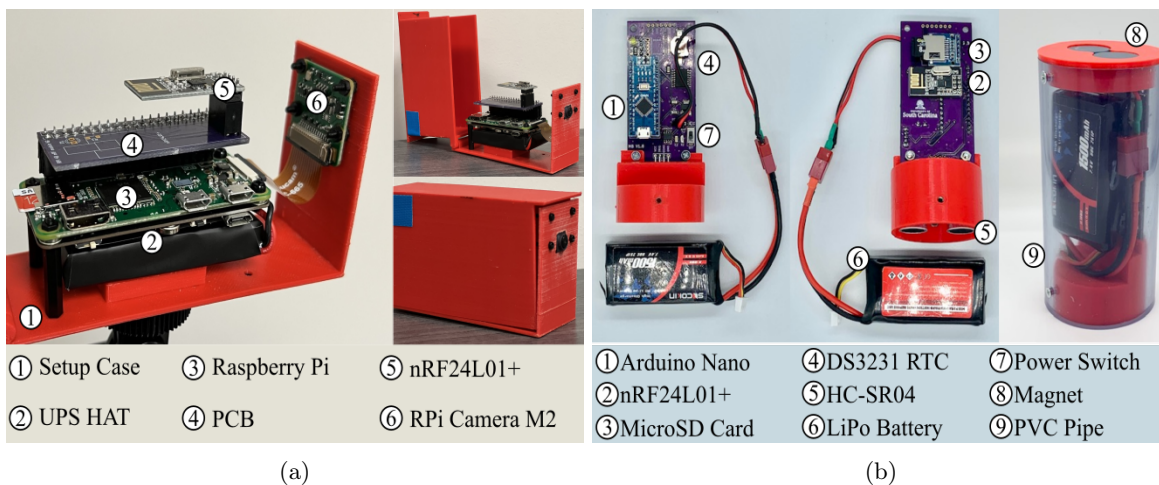


Figure 3: Data acquisition devices. (a) Beena, run by Raspberry Pi (Zero W) for capturing time-lapse images of the river scene; and (b) Aava, run by Arduino Nano for measuring water level correspondence.

210 A dataset for semantic segmentation was created by collecting images from a specific region of interest
 211 at different times of the day and under various flow regimes. This dataset includes 1,172 images, with
 212 manual annotations of the streamflow in the creek for all of them. The dataset is further divided into
 213 812 training images, 124 validation images, and 236 testing images.

214 4.2 Deep Learning Model for Water Segmentation

215 The water extent can be automatically determined on the 2D image plane with the help of DL-based
 216 models. The task of semantic segmentation was applied within the framework of this study to delineate
 217 the water line on the left and right banks of the channel. Three different DL-based models were trained
 218 and tested in this study. PSPNet, the first model, is a CNN-based semantic segmentation multi-scale
 219 network which can better learn the global context representation of a scene [Zhao et al., 2017]. ResNet-
 220 101 [He et al., 2016] was used as the backbone of this model to encode input images into the features.
 221 ResNet architecture takes the advantage of “Residual blocks” that assist the flow of gradients during
 222 the training stage allowing effective training of deep models even up to hundreds of layers. These
 223 extracted features are then fed into a pyramid pooling module in which feature maps produced by
 224 small to large kernels are concatenated to distinguish patterns of different scales [Minaee et al., 2021].

225 TransUNet, the second model, is a U-shaped architecture that employs a hybrid of CNN and Trans-
 226 formers as the encoder to leverage both the local and global contexts for precise localization and
 227 pixel-wise classification [Chen et al., 2021]. In the encoder part of the network, CNN is first used as a
 228 feature extractor to generate a feature map for the input image, which is then fed into Transformers
 229 to extract long-range dependencies. The resulting features are upsampled in the decoding path and
 230 combined with detailed high-resolution spatial information skipped from the CNN to make estimations
 231 on each pixel of the input image.

232 SegFormer, the third model, unifies a novel hierarchical Transformer, which does not require the posi-
 233 tional encodings used in standard Transformers, and MultiLayer Perceptron (MLP) performs efficient

234 segmentation [Xie et al., 2021]. The hierarchical Transformer introduced in the encoder of this archite-
 235 ture gives the model the attention ability to multiscale features (high-resolution fine and low-resolution
 236 coarse information) in the spatial input without the need for positional encodings that may adversely
 237 affect a models performance when testing on a different resolution from training. Moreover, unlike
 238 other segmentation models that typically use deconvolutions in the decoder path, a lightweight MLP
 239 is employed as the decoder of this network that inputs the features extracted at different stages of
 240 the encoder to generate a prediction map faster and more efficiently. Two different variants, including
 241 SegFormer-B0 and SegFormer-B5, were applied in this study. The configuration of the models imple-
 242 mented in this study is elaborated in Table 1. The total number of parameters (Params), occupied
 243 memory size on GPU (Total Size), and input image size (Batch Size) are reported in Million (M),
 244 Megabyte (MB), and Batch size \times Height \times Width \times Channel (B, H, W, C) respectively.

Table 1: The configuration of models trained and tested in this study.

Model Names	Params (M)	Total Size (MB)	Batch Size (B, H, W, C)	Loss Function	Optimizer	LR
PSPNet	66.2	7,178	$2\times 500\times 500\times 3$	Binary Cross Entropy	SGD	2.50E-04
TransUNet	20.1	6,017	$2\times 448\times 448\times 3$	Cross Entropy + Dice	SGD	2.50E-04
SegFormer-B0	3.7	2,217	$2\times 512\times 512\times 3$	Cross Entropy	AdamW	6.00E-05
SegFormer-B5	82.0	27,666	$2\times 1024\times 1024\times 3$	Cross Entropy	AdamW	6.00E-05

245 The models were implemented using PyTorch. During the training procedure, the loss function, opti-
 246 mizer, and learning rate were set individually for each model based on the results of preliminary runs
 247 used to find the optimal hyperparameters. In the case of PSPNet and TransUNet, the base learn-
 248 ing rate was set to 2.5×10^{-4} and decayed using the poly policy [Zhao et al., 2017]. These networks
 249 were optimized using stochastic gradient descent (SGD) with a momentum of 0.9 and weight decay of
 250 0.0001. For SegFormer (B0 and B5), a constant learning rate of 6.0×10^{-5} was used, and the networks
 251 were trained with the AdamW optimizer [Loshchilov and Hutter, 2017]. All networks were trained for
 252 30 epochs with a batch size of two. The training data for PSPNet and TransUNet were augmented
 253 with horizontal flipping, random scaling, and random cropping.

254 4.3 Projective Geometry

255 In this study, CV techniques are used for different purposes. First, CV models were used for camera
 256 calibration. They include focal length, optical center, radial distortion, camera rotation, and transla-
 257 tion. These parameters provide the information (parameters or coefficients) about the camera that is
 258 required to determine the relationship between 3D object points in the real-world coordinate system
 259 and its corresponding 2D projection (pixel) in the image captured by that calibrated camera. Gen-
 260 erally, camera calibration models estimate two kinds of parameters. First, the internal parameters of
 261 the camera (e.g., focal length, optical center, and radial distortion coefficients of the lens). Second,
 262 external parameters (refer to the orientation– rotation and translation– of the camera with respect to
 263 the real-world coordinate system.

264 To estimate the camera intrinsic parameters, OpenCV built-in was applied for camera calibration using
 265 a 2D checkerboard [Bradski, 2000]. Intrinsic parameters are specific to a camera. The focal length (f_x ,
 266 f_y) and optical centers (c_x, c_y) can be used to create a camera matrix. The camera matrix is unique
 267 to a specific camera, so once calculated, it can be reused on other images taken by the same camera
 268 (Equation 1). It is expressed as a 3×3 matrix:

$$\text{camrea matrix} = \begin{bmatrix} f_x & 0 & c_x \\ 0 & f_y & c_y \\ 0 & 0 & 1 \end{bmatrix} \quad (1)$$

269 The camera extrinsic parameters were determined using the pose estimation problem which consists
 270 in solving for the rotation, and translation that minimizes the reprojection error from 2D-3D point
 271 correspondences [Marchand et al., 2015]. For this purpose, the iterative method was applied which
 272 is based on a Levenberg-Marquardt optimization. In this task the function finds such a pose that

273 minimizes reprojection error, that is the sum of squared distances between the observed projections
 274 “image point” and the projected “object points.” The initial solution for non-planar 3D object points
 275 needs at least six points and uses the Direct Linear Transformation (DLT) algorithm.

$$\begin{bmatrix} u \\ v \\ 1 \end{bmatrix} = \underbrace{\begin{bmatrix} f_x & 0 & c_x & 0 \\ 0 & f_y & c_y & 0 \\ 0 & 0 & 1 & 0 \end{bmatrix}}_{\mathbf{K}} \underbrace{\begin{bmatrix} r_{11} & r_{12} & r_{13} & t_x \\ r_{21} & r_{22} & r_{23} & t_y \\ r_{31} & r_{32} & r_{33} & t_z \\ 0 & 0 & 0 & 1 \end{bmatrix}}_{[\mathbf{R}|\mathbf{t}]} \begin{bmatrix} X_w \\ Y_w \\ Z_w \\ 1 \end{bmatrix} \quad (2)$$

276 Equation 2 represents “Projection Matrix” consisting of two parts– the intrinsic matrix (\mathbf{K}) that
 277 contains the intrinsic parameters and the extrinsic matrix ($[\mathbf{R} \mid \mathbf{t}]$) that is a combination of 3×3
 278 rotation matrix \mathbf{R} and a 3×1 translation \mathbf{t} vector.

279 2D points are represented with ArUco markers’ pixel coordinates on the 2D image plane, and cor-
 280 responding 3D object points are measured by the total station. Having at least six 3D-2D point
 281 correspondences, the spatial position and orientation of the camera can be estimated for each setup
 282 deployment. After retrieving all the necessary parameters, a full-perspective camera model can be
 283 generated. Using this model, the 3D point cloud is projected on the 2D image plane. The projected
 284 (2D) point cloud can represent 3D real-world coordinates of the nearest 2D pixel correspondence on
 285 the image plane.

286 4.4 Machine Learning for Image Measurements

287 Using the projection matrix, the 3D point cloud is projected on the 2D image plane (see Figure 4). The
 288 projected (2D) point cloud is intersected with the water line pixels, the output of the DL-based model
 289 (Module 1), to find the nearest point cloud coordinate. To achieve this objective, we utilize the K-
 290 Nearest Neighbors (KNN) algorithm. Notably, the indices of the selected points remain consistent for
 291 both the 3D point cloud and the projected (2D) correspondences. As a result, by utilizing the indices
 292 of the chosen projected (2D) points, the corresponding real-world 3D coordinates can be retrieved.

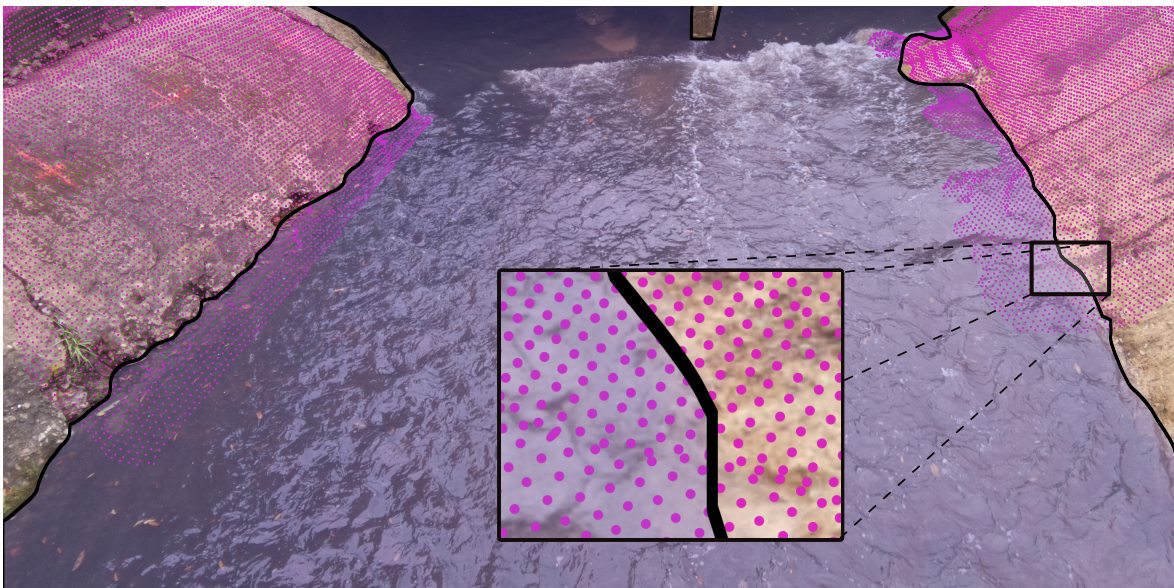


Figure 4: KNN is used to find the nearest projected (2D) point cloud (magenta dots) to the water line (black line) on the image plane.

5 Results and Discussion

The results of this study are presented in two sections. First, the performance of DL-based models is discussed. Then, in the second section, the performance of the proposed framework is evaluated for five different deployments.

5.1 DL-based Models Results

The performance of DL-based models for the task of semantic segmentation is evaluated and compared in this section. Since the proposed dataset includes just two classes, “river” and “non-river”, “non-river” was omitted from the evaluation process, and the performance of models is only reported for the “river” class of the test set. The class-wise intersection over union (IoU) and the per-pixel accuracy (ACC) were considered the main evaluation metrics in this study. According to Table 2, both variants of SegFormer– SegFormer-B0, and SegFormer-B5– outperform other semantic segmentation networks on the test set. Considering the models’ configurations detailed in Table 1, SegFormer-B0 can be considered the most efficient DL-based network, as it is comprised of only 3.7 M trainable parameters and occupies just 2,217 Megabytes of GPU ram during training. In Figure 5, four different visual representations of the models’ performance on the validation set of the proposed dataset are presented. Since the water level is estimated by intersecting the water line on river banks with the projected (2D) point cloud, precise delineation of the water line is of utmost importance to achieve better results in the following steps. This means that estimating the correct location of the water line on creek banks in each time-lapse image plays a more significant role than performance metrics in this study. Taking the quality of water line detection into account and based on the visual representations shown in Figure 5, SegFormers’ variants still outperform DL-based approaches. In this regard, a comparison of PSPNet and TransUNet showed that PSPNet can delineate the water line more clearly, while the segmented area is more integrated for TransUNet outputs.

Table 2: The performance metrics of different DL-based approaches.

Model Names	IoU (River)	ACC (River)
PSPNet	94.88%	95.84%
TransUNet	93.54%	96.89%
SegFormer-B0	99.38%	99.77%
SegFormer-B5	99.55%	99.81%

CNNs are typically limited by the nature of their convolution operations, leading to architecture-specific issues such as locality [Geirhos et al., 2018a]. Consequently, CNN-based models may achieve high accuracy on training data, but their performance can decrease considerably on unseen data. Additionally, compared to Transformer-based networks, they perform poorly at detecting semantics that requires combining long- and short-range dependencies. Transformers can relax the biases of DL-based models inducted by Convolutional operations, achieving higher accuracy in localization of target semantics and pixel-level classification with lower fluctuations in varied situations through the leverage of both local and global cues [Naseer et al., 2021]. Yet, various transformer-based networks may perform differently depending on the targeted task and the network’s architecture. TransUNet adopts Transformers as part of its backbone; however, Transformers generate single-scale low-resolution features as output [Xie et al., 2021], which may limit the accuracy when multi-scale objects or single objects with multi-scale features are segmented. The problem of producing single-scale features in standard Transformers is addressed in SegFormer variants through the use of a novel hierarchical Transformer encoder [Xie et al., 2021]. This approach has resulted in human-level accuracy being achieved by Segformer-B0 and -B5 in the delineation of the water line, as shown in Figure 5. The predicted masks are in satisfactory agreement with the manually annotated images.

5.2 Water Level Estimation

This section reports the framework performance based on several deployments in the field. The performance results are separately shown for the left and right banks and compared with ultrasonic sensor data as the ground truth. The ultrasonic sensor was evaluated previously that documented an average

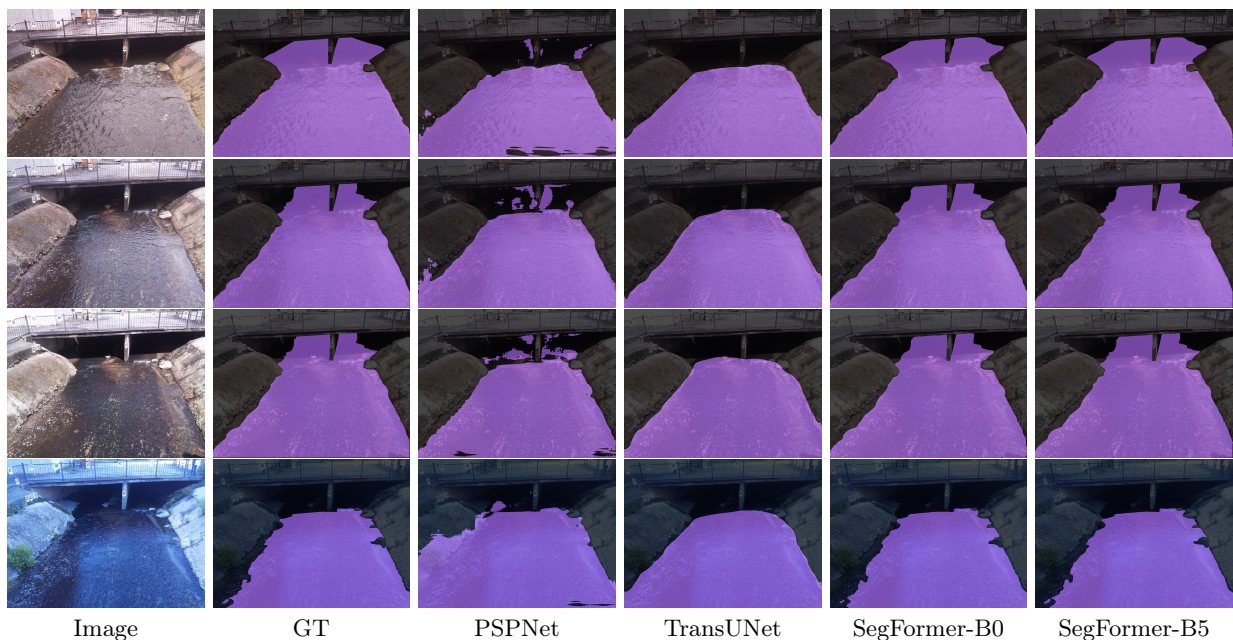


Figure 5: Visual representations of different DL-based image segmentation approaches on the validation dataset.

336 distance error of 6.9 mm [Smith et al., 2022]. Four different efficiency criteria including coefficient of
 337 determination (R^2), Nash-Sutcliffe Efficiency (NSE), Root Mean Square Error (RMSE), and Percent
 338 bias (PBIAS) are reported in Table 3. R^2 , as the most representative metric, emphasizes how much
 339 of the observed dispersion can be explained by the prediction. However, if the model systematically
 340 over- or under-estimates the results, R^2 will still be close to 1.0 as it only takes dispersion into ac-
 341 count [Krause et al., 2005]. NSE, a traditional metric used in hydrology is also used to summarize model
 342 performance. NSE normalizes model performance into an interpretable scale and is commonly used to
 343 differentiate between ‘good’ and ‘bad’ models [Knoben et al., 2019]. RMSE represents the square root
 344 of the average of squares of the errors, the differences between predicted values and observed values.
 345 The PBIAS of estimated water level, compared against the ultrasonic sensor data was also used to
 346 show where the two estimates are close to each other and where they significantly diverge [Lin et al.,
 347 2020].

Table 3: The performance metrics of the framework for five different days of setup deployment.

Deployment Date	Position	Metrics			
		R^2	NSE	RMSE	PBIAS
Aug/17/2022	Left Bankline	0.8019	0.5258	0.0409	10.6401
	Right Bankline	0.7932	0.7541	0.0294	-0.4848
Aug/19/2022	Left Bankline	0.7701	0.5713	0.0647	16.1015
	Right Bankline	0.9678	0.9588	0.0201	-3.4752
Aug/25/2022	Left Bankline	0.7690	0.5700	0.0435	-7.7091
	Right Bankline	0.8922	0.8711	0.0238	-1.7738
Nov/10/2022	Left Bankline	0.9461	0.8129	0.0511	-13.1183
	Right Bankline	0.9857	0.9790	0.0171	-1.5210
Nov/11/2022	Left Bankline	0.9588	0.8881	0.0397	-10.3656
	Right Bankline	0.9855	0.9829	0.0155	-1.7987

348 The setup was deployed on several rainy days. In addition to Table 3, the results of each deployment are
 349 visually demonstrated in Figure 6. The scatter plots show the relationships between the ground truth
 350 data (measured by the ultrasonic sensor), and the banks of the river. The scatter plots visually present

351 whether the camera readings overestimate or underestimate the ground truth data. Moreover, the time-
352 series plot of water level is shown for each deployment separately. A hydrograph, showing changes in
353 the water level of a stream over time can be a useful tool for demonstrating whether camera readings
354 can satisfactorily capture the response of a catchment area to rainfall. The proposed framework can
355 be evaluated in terms of its ability to accurately track and identify important characteristics of a flood
356 wave, such as the rising limb, peak, and recession limb.

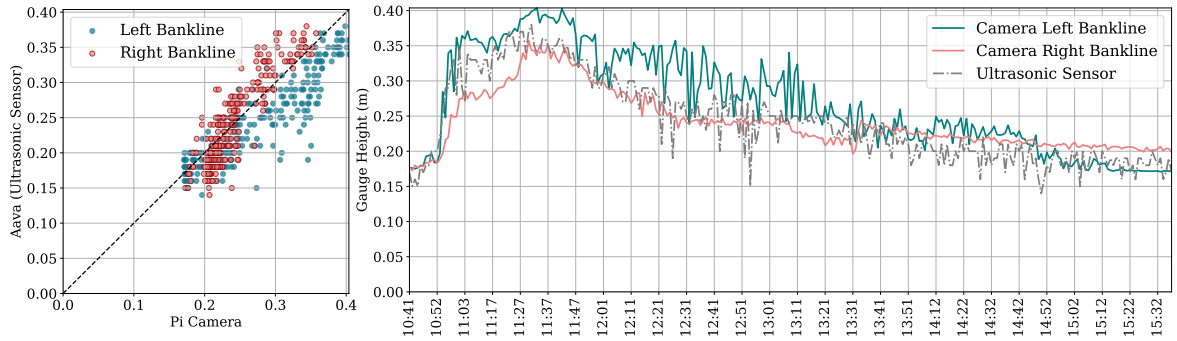
357 The first deployment was done on Aug 17, 2022 (see Figure 6a). The initial water level of the base
358 flow and parts of the rising limb were not captured in this deployment. Table 3 shows that the
359 performance results of the right bank camera readings are better than those of the left bank. R^2 for
360 both banks was about 0.80 showing a strongly related correlation between the water level estimated by
361 the framework and ground truth data. Figure 6a shows how the left and right bank camera readings
362 perform during the rising limb; the right bank camera readings still underestimated the water level
363 during this time frame, and during the recession limb, the left bank camera readings overestimated
364 the water level. However, the hydrograph plot shows that both left and right bank camera readings
365 were able to capture the peak water level.

366 The second deployment was done on Aug 19, 2022. In this deployment, all segments of the hydrograph
367 were captured. According to Table 3, the performance of the right bank camera readings was better
368 than the left bank one; more than 0.95 was reported for R^2 and NSE of the right bankline. Figure 6b
369 shows during the rising limb and crest segment both banks estimated the water level similar to ground
370 truth. During the recession limb, the right bank water level estimation kept coincident with ground
371 truth, while the left bank overestimated the water level. The third deployment was on Aug 25, 2022.
372 This time water level of the recession limb and the following base flow were captured (see Figure 6c).
373 The right bank camera readings with R^2 of 0.89 performed better than the left bank. This time, left
374 bank camera readings underestimated the water level over the recession limb, but during the following
375 base flow, the water level was estimated correctly by cameras on both banks.

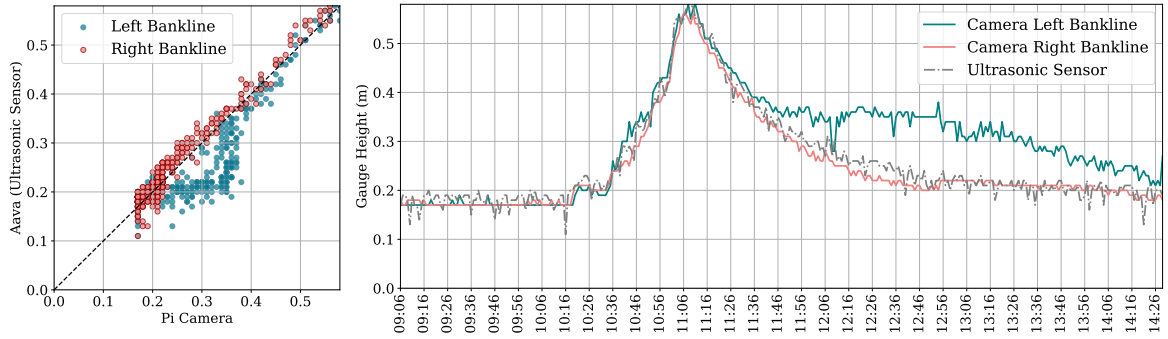
376 The results indicate that the right bank camera readings performed better than the left bank. Further
377 investigation of the field conditions revealed that stream erosion had a more significant impact on the
378 concrete surface of the left bank, resulting in patches and holes that were not scanned by the iPhone
379 LiDAR. As a result, the KNN algorithm used to find the nearest (2D) point cloud coordinates to the
380 water line could not accurately represent the corresponding real-world coordinates of these locations.
381 Figure 7 shows a box plot and scatter plot of the estimated water level for a time-lapse image captured
382 at 13:29 on Aug 19, 2022. The patches and holes on the left bank surface caused instability in water
383 level estimation for the region of interest. The box plot of the left bank (Cam-L-BL) was taller than
384 that of the right bank (Cam-R-BL), indicating that the estimated water level was spread over larger
385 values in the left bank due to the presence of these irregularities.

386 After analyzing the initial results, the deployable setups were modified to enhance the quality of data
387 collection. The programming code of the Arduino device, Aava, was modified to measure five different
388 records for water level, each time it is triggered by the camera device, Beena, and transmit the average
389 distance to the Raspberry Pi device. This modification decreased the number of noise spikes in the
390 measured data and allowed a better comparison between camera readings and ground truth data.
391 The case of the camera device, Beena, was redesigned to protect the single board against rain without
392 requiring an umbrella which makes the camera setup unstable in stormy weather and causes a decrease
393 in the precision of measurements. Moreover, an opening is incorporated into the redesigned case to
394 connect an external power bank to enhance the run time. Finally, the viewpoint of the camera was
395 subtly shifted to the right to adjust the share of the river banks on the camera's field of view.

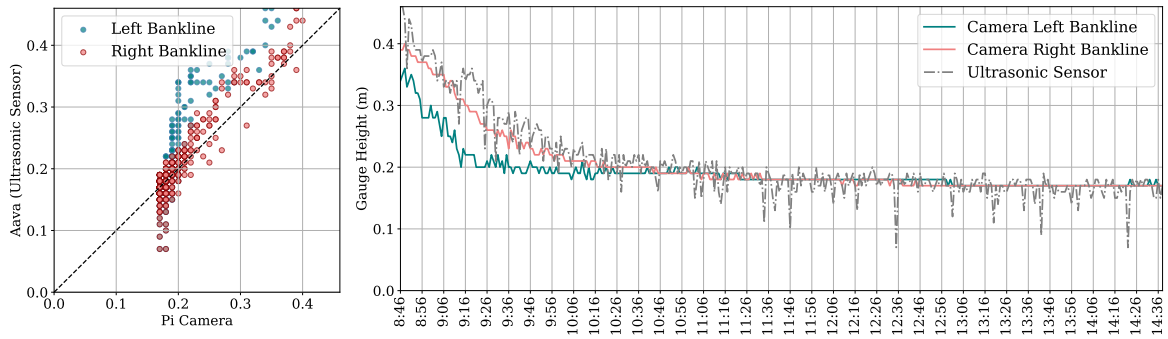
396 The results of the deployments on Nov 10, 2022, and Nov 11, 2022, demonstrate that modifications
397 to the setup have significantly improved the results of the left bank (as shown in Table 3). NSE
398 improved from approximately 0.55 for the first three setup deployments to over 0.80 for the modified
399 deployments. Figure 8 shows the setup performances during all segments of the flood wave. The peaks
400 were captured by the right bankline on both deployment dates, and there was no effect of noisy spikes
401 on either camera readings or ground truth data. However, the right bank images still underestimated
402 the water level during the rainstorms.



(a)



(b)



(c)

Figure 6: Scatter plot and time series plot for estimated water level by the proposed framework and measured by the ultrasonic sensor for setup deployment on (a) Aug 17, 2022 (b) Aug 19, 2022, and (c) Aug 25, 2022.

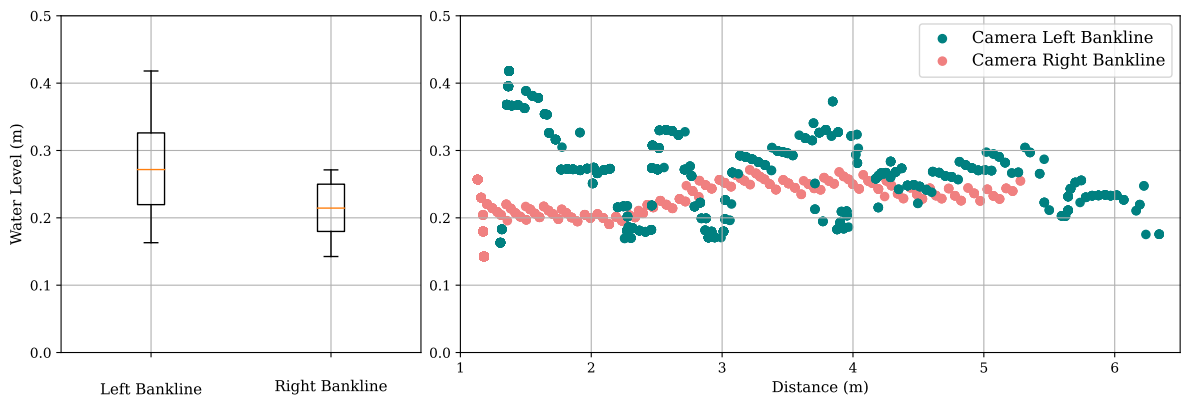


Figure 7: Water level fluctuation along both left and right banks for the flow regime for an image captured at 13:29 on Aug 19, 2022.

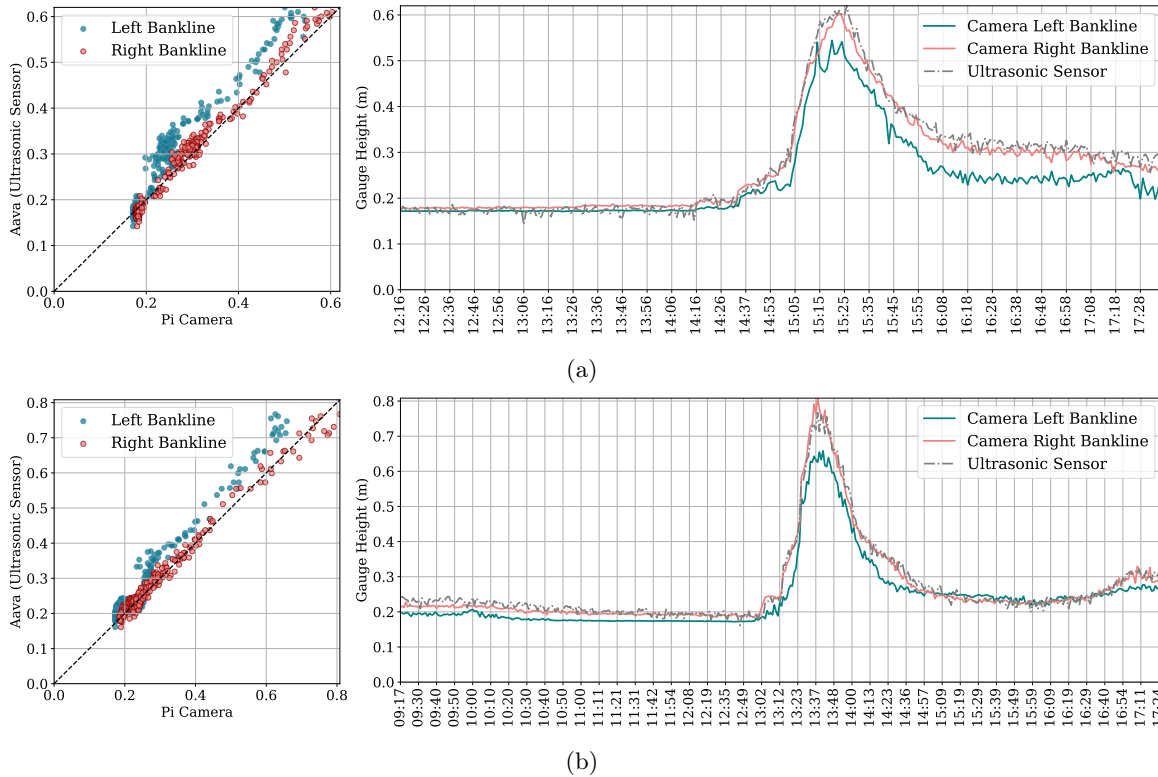


Figure 8: Scatter plot and time series plot for estimated water level by the proposed framework and measured by the ultrasonic sensor for setup deployment on (a) Nov 10, 2022, and (b) Nov 11, 2022.

6 Conclusion

This study introduced Eye of Horus, a vision-based framework for hydrologic monitoring and measuring real-time water-related parameters, e.g., water level, from surveillance images captured during flood events. Time-lapse images and real water level correspondences were collected by Raspberry Pi camera and Arduino HC-SR05 ultrasonic sensor, respectively. Moreover, Computer Vision and Deep Learning techniques were used for semantic segmentation of water surface within the captured images and for reprojecting the 3D point cloud constructed with an iPhone LiDAR scanner, on the (2D) image plane. Eventually, the K-Nearest Neighbor algorithm was used to intersect the projected (2D) point cloud with the water line pixels extracted from the output of the Deep Learning model, to find the real-world 3D coordinates.

A vision-based framework offers a new alternative to current hydrologic data collection and real-time monitoring systems. Hydrological models require geometric information for estimating discharge routing parameters, stage, and flood inundation maps. However, determining bankfull characteristics is a challenge due to natural or anthropogenic down-cutting of streams. Using visual sensing, stream depth, water velocity, and instantaneous streamflow at bankfull stage can be reliably measured.

7 Data Availability Statement

The framework and codes developed and used in this study are available online in the GitHub repository (<https://github.com/smhassanerfani/horus>).

References

Douglas E Alsdorf, Ernesto Rodríguez, and Dennis P Lettenmaier. Measuring surface water from space. *Reviews of Geophysics*, 45(2), 2007.

- 424 Vijay Badrinarayanan, Ankur Handa, and Roberto Cipolla. Segnet: A deep convolutional encoder-
425 decoder architecture for robust semantic pixel-wise labelling. *arXiv preprint arXiv:1505.07293*, 2015.
- 426 G. Bradski. The OpenCV Library. *Dr. Dobb's Journal of Software Tools*, 2000.
- 427 Jieneng Chen, Yongyi Lu, Qihang Yu, Xiangde Luo, Ehsan Adeli, Yan Wang, Le Lu, Alan L Yuille,
428 and Yuyin Zhou. Transunet: Transformers make strong encoders for medical image segmentation.
429 *arXiv preprint arXiv:2102.04306*, 2021.
- 430 Liang-Chieh Chen, George Papandreou, Iasonas Kokkinos, Kevin Murphy, and Alan L Yuille. Deeplab:
431 Semantic image segmentation with deep convolutional nets, atrous convolution, and fully connected
432 crfs. *IEEE Trans. Pattern Anal. Mach. Intell.*, 40(4):834–848, 2017.
- 433 Andrea De Cesarei, Shari Cavicchi, Giampaolo Cristadoro, and Marco Lippi. Do humans and deep con-
434 volutional neural networks use visual information similarly for the categorization of natural scenes?
435 *Cognitive Science*, 45(6):e13009, 2021.
- 436 Samuel Dodge and Lina Karam. A study and comparison of human and deep learning recognition
437 performance under visual distortions. In *Int. Conf. Comput. Communication and Networks*, pages
438 1–7. IEEE, 2017.
- 439 Alexey Dosovitskiy, Lucas Beyer, Alexander Kolesnikov, Dirk Weissenborn, Xiaohua Zhai, Thomas
440 Unterthiner, Mostafa Dehghani, Matthias Minderer, Georg Heigold, Sylvain Gelly, et al. An image
441 is worth 16x16 words: Transformers for image recognition at scale. *arXiv preprint arXiv:2010.11929*,
442 2020.
- 443 Melanie Elias, Anette Eltner, Frank Liebold, and Hans-Gerd Maas. Assessing the influence of temper-
444 ature changes on the geometric stability of smartphone-and raspberry pi cameras. *Sensors*, 20(3):
445 643, 2020.
- 446 Anette Eltner and Danilo Schneider. Analysis of different methods for 3d reconstruction of natural
447 surfaces from parallel-axes uav images. *The Photogrammetric Record*, 30(151):279–299, 2015.
- 448 Anette Eltner, Andreas Kaiser, Carlos Castillo, Gilles Rock, Fabian Neugirg, and Antonio Abellán.
449 Image-based surface reconstruction in geomorphometry—merits, limits and developments. *Earth
450 Surface Dynamics*, 4(2):359–389, 2016.
- 451 Anette Eltner, Melanie Elias, Hannes Sardemann, and Diana Spieler. Automatic image-based water
452 stage measurement for long-term observations in ungauged catchments. *Water Resources Research*,
453 54(12):10–362, 2018.
- 454 Anette Eltner, Patrik Olā Bressan, Thales Akiyama, Wesley Nunes Gonçalves, and Jose Marcato Ju-
455 nior. Using deep learning for automatic water stage measurements. *Water Resources Research*, 57
456 (3):e2020WR027608, 2021.
- 457 Seyed Mohammad Hassan Erfani, Zhenyao Wu, Xinyi Wu, Song Wang, and Erfan Goharian. Atlantis:
458 A benchmark for semantic segmentation of waterbody images. *Environmental Modelling & Software*,
459 149:105333, 2022.
- 460 David A Forsyth and Jean Ponce. *Computer vision: a modern approach*. prentice hall professional
461 technical reference, 2002.
- 462 Laurent Froideval, Kevin Pedoja, Franck Garestier, Pierre Moulon, Christophe Conessa, Xavier Pellerin
463 Le Bas, Kalil Traoré, and Laurent Benoit. A low-cost open-source workflow to generate georeferenced
464 3d sfm photogrammetric models of rocky outcrops. *The Photogrammetric Record*, 34(168):365–384,
465 2019.
- 466 Jun Fu, Jing Liu, Haijie Tian, Yong Li, Yongjun Bao, Zhiwei Fang, and Hanqing Lu. Dual attention
467 network for scene segmentation. In *IEEE Conf. Comput. Vis. Pattern Recog.*, pages 3146–3154,
468 2019.
- 469 Asmamaw Gebrehiwot, Leila Hashemi-Beni, Gary Thompson, Parisa Kordjamshidi, and Thomas E
470 Langan. Deep convolutional neural network for flood extent mapping using unmanned aerial vehicles
471 data. *Sensors*, 19(7):1486, 2019.

- 472 Robert Geirhos, Patricia Rubisch, Claudio Michaelis, Matthias Bethge, Felix A Wichmann, and
473 Wieland Brendel. Imagenet-trained cnns are biased towards texture; increasing shape bias improves
474 accuracy and robustness. *arXiv preprint arXiv:1811.12231*, 2018a.
- 475 Robert Geirhos, Carlos RM Temme, Jonas Rauber, Heiko H Schütt, Matthias Bethge, and Felix A
476 Wichmann. Generalisation in humans and deep neural networks. *Adv. Neural Inform. Process. Syst.*,
477 31, 2018b.
- 478 Robert Geirhos, Kristof Meding, and Felix A Wichmann. Beyond accuracy: quantifying trial-by-trial
479 behaviour of cnns and humans by measuring error consistency. *Adv. Neural Inform. Process. Syst.*,
480 33:13890–13902, 2020.
- 481 Troy E Gilmore, François Birgand, and Kenneth W Chapman. Source and magnitude of error in an
482 inexpensive image-based water level measurement system. *Journal of hydrology*, 496:178–186, 2013.
- 483 Christoph Gollob, Tim Ritter, Ralf Kraßnitzer, Andreas Tockner, and Arne Nothdurft. Measurement
484 of forest inventory parameters with Apple iPad pro and integrated LiDAR technology. *Remote
485 Sensing*, 13(16):3129, 2021.
- 486 Michael F Goodchild. Citizens as sensors: the world of volunteered geography. *GeoJournal*, 69(4):
487 211–221, 2007.
- 488 Kaiming He, Xiangyu Zhang, Shaoqing Ren, and Jian Sun. Deep residual learning for image recogni-
489 tion. In *IEEE Conf. Comput. Vis. Pattern Recog.*, pages 770–778, 2016.
- 490 Jeff Howe. *Crowdsourcing: How the power of the crowd is driving the future of business*. Random
491 House, 2008.
- 492 Zilong Huang, Xinggang Wang, Lichao Huang, Chang Huang, Yunchao Wei, and Wenyu Liu. Ccnet:
493 Criss-cross attention for semantic segmentation. In *Int. Conf. Comput. Vis.*, pages 603–612, 2019.
- 494 J Kim, Y Han, and H Hahn. Embedded implementation of image-based water-level measurement
495 system. *IET computer vision*, 5(2):125–133, 2011.
- 496 Tyler V King, Bethany T Neilson, and Mitchell T Rasmussen. Estimating discharge in low-order rivers
497 with high-resolution aerial imagery. *Water Resources Research*, 54(2):863–878, 2018.
- 498 Wouter JM Knoben, Jim E Freer, and Ross A Woods. Inherent benchmark or not? comparing nash-
499 sutcliffe and kling-gupta efficiency scores. *Hydrology and Earth System Sciences*, 23(10):4323–4331,
500 2019.
- 501 Peter Krause, DP Boyle, and Frank Bäse. Comparison of different efficiency criteria for hydrological
502 model assessment. *Advances in Geosciences*, 5:89–97, 2005.
- 503 LAAN LABS. 3D Scanner App – LiDAR Scanner for iPad Pro & iPhone Pro. Available online:
504 <https://3dscannerapp.com/>, 2022. Accessed on Sep 16, 2022.
- 505 Xia Li, Zhisheng Zhong, Jianlong Wu, Yibo Yang, Zhouchen Lin, and Hong Liu. Expectation-
506 maximization attention networks for semantic segmentation. In *Int. Conf. Comput. Vis.*, pages
507 9167–9176, 2019.
- 508 Zhenlong Li, Cuizhen Wang, Christopher T Emrich, and Diansheng Guo. A novel approach to leverag-
509 ing social media for rapid flood mapping: a case study of the 2015 south carolina floods. *Cartography
510 and Geographic Information Science*, 45(2):97–110, 2018.
- 511 Guosheng Lin, Anton Milan, Chunhua Shen, and Ian Reid. Refinenet: Multi-path refinement networks
512 for high-resolution semantic segmentation. In *IEEE Conf. Comput. Vis. Pattern Recog.*, pages 1925–
513 1934, 2017.
- 514 Peirong Lin, Ming Pan, George H Allen, Renato Prata de Frasson, Zhenzhong Zeng, Dai Yamazaki,
515 and Eric F Wood. Global estimates of reach-level bankfull river width leveraging big data geospatial
516 analysis. *Geophysical Research Letters*, 47(7):e2019GL086405, 2020.

- 517 Ze Liu, Yutong Lin, Yue Cao, Han Hu, Yixuan Wei, Zheng Zhang, Stephen Lin, and Baining Guo.
518 Swin transformer: Hierarchical vision transformer using shifted windows. In *Int. Conf. Comput.*
519 *Vis.*, pages 10012–10022, 2021.
- 520 Shi-Wei Lo, Jyh-Horng Wu, Fang-Pang Lin, and Ching-Han Hsu. Visual sensing for urban flood
521 monitoring. *Sensors*, 15(8):20006–20029, 2015.
- 522 Jonathan Long, Evan Shelhamer, and Trevor Darrell. Fully convolutional networks for semantic seg-
523 mentation. In *IEEE Conf. Comput. Vis. Pattern Recog.*, pages 3431–3440, 2015.
- 524 Ilya Loshchilov and Frank Hutter. Decoupled weight decay regularization. *arXiv preprint*
525 *arXiv:1711.05101*, 2017.
- 526 Gregor Luetzenburg, Aart Kroon, and Anders A Bjørk. Evaluation of the apple iphone 12 pro lidar
527 for an application in geosciences. *Scientific reports*, 11(1):1–9, 2021.
- 528 Eric Marchand, Hideaki Uchiyama, and Fabien Spindler. Pose estimation for augmented reality: a
529 hands-on survey. *IEEE Trans. Pattern Anal. Mach. Intell.*, 22(12):2633–2651, 2015.
- 530 Shervin Minaee, Yuri Y Boykov, Fatih Porikli, Antonio J Plaza, Nasser Kehtarnavaz, and Demetri
531 Terzopoulos. Image segmentation using deep learning: A survey. *IEEE Trans. Pattern Anal. Mach.*
532 *Intell.*, 2021.
- 533 Martin Mokroš, Tomáš Mikita, Arunima Singh, Julián Tomaščík, Juliána Chudá, Piotr Wężyk, Karel
534 Kuželka, Peter Surový, Martin Klimánek, Karolina Zięba-Kulawik, et al. Novel low-cost mobile
535 mapping systems for forest inventories as terrestrial laser scanning alternatives. *International Journal*
536 *of Applied Earth Observation and Geoinformation*, 104:102512, 2021.
- 537 Mohamed M Morsy, Jonathan L Goodall, Fadi M Shatnawi, and Michael E Meadows. Distributed
538 stormwater controls for flood mitigation within urbanized watersheds: case study of rocky branch
539 watershed in columbia, south carolina. *Journal of Hydrologic Engineering*, 21(11):05016025, 2016.
- 540 Matthew Moy de Vitry, Simon Kramer, Jan Dirk Wegner, and João P Leitão. Scalable flood level
541 trend monitoring with surveillance cameras using a deep convolutional neural network. *Hydrology*
542 *and Earth System Sciences*, 23(11):4621–4634, 2019.
- 543 Muhammad Muzammal Naseer, Kanchana Ranasinghe, Salman H Khan, Munawar Hayat, Fahad
544 Shahbaz Khan, and Ming-Hsuan Yang. Intriguing properties of vision transformers. *Adv. Neural*
545 *Inform. Process. Syst.*, 34:23296–23308, 2021.
- 546 Hyeonwoo Noh, Seunghoon Hong, and Bohyung Han. Learning deconvolution network for semantic
547 segmentation. In *Int. Conf. Comput. Vis.*, pages 1520–1528, 2015.
- 548 RJ Pally and S Samadi. Application of image processing and convolutional neural networks for flood
549 image classification and semantic segmentation. *Environmental Modelling & Software*, 148:105285,
550 2022.
- 551 George Panteras and Guido Cervone. Enhancing the temporal resolution of satellite-based flood ex-
552 tent generation using crowdsourced data for disaster monitoring. *International Journal of Remote*
553 *Sensing*, 39(5):1459–1474, 2018.
- 554 E Schnebele, G Cervone, and N Waters. Road assessment after flood events using non-authoritative
555 data. *Natural Hazards and Earth System Sciences*, 14(4):1007, 2014.
- 556 Elyas Asadi Shamsabadi, Chang Xu, and Daniel Dias-da Costa. Robust crack detection in masonry
557 structures with transformers. *Measurement*, 200:111590, 2022.
- 558 Corinne Smith, Joud Satme, Jacob Martin, Austin R.J. Downey, Nikolaos Vitzilaios, and Jasim Imran.
559 UAV rapidly-deployable stage sensor with electro-permanent magnet docking mechanism for flood
560 monitoring in undersampled watersheds. *HardwareX*, 12:e00325, oct 2022. doi: 10.1016/j.ohx.2022.
561 e00325.
- 562 Stefano Tavani, Andrea Billi, Amerigo Corradetti, Marco Mercuri, Alessandro Bosman, Marco Cuf-
563 faro, Thomas Seers, and Eugenio Carminati. Smartphone assisted fieldwork: Towards the digital

564 transition of geoscience fieldwork using lidar-equipped iphones. *Earth-Science Reviews*, 227:103969,
565 2022.

566 Ryota Tsubaki, Ichiro Fujita, and Shiho Tsutsumi. Measurement of the flood discharge of a small-sized
567 river using an existing digital video recording system. *Journal of Hydro-environment Research*, 5
568 (4):313–321, 2011.

569 D Phil Turnipseed and Vernon B Sauer. Discharge measurements at gaging stations. Technical report,
570 US Geological Survey, 2010.

571 Ashish Vaswani, Noam Shazeer, Niki Parmar, Jakob Uszkoreit, Llion Jones, Aidan N Gomez, Łukasz
572 Kaiser, and Illia Polosukhin. Attention is all you need. *Adv. Neural Inform. Process. Syst.*, 30, 2017.

573 Maximilian Vogt, Adrian Rips, and Claus Emmelmann. Comparison of ipad pro®’s lidar and
574 truedepth capabilities with an industrial 3d scanning solution. *Technologies*, 9(2):25, 2021.

575 Matthew J Westoby, James Brasington, Niel F Glasser, Michael J Hambrey, and Jennifer M Reynolds.
576 ‘structure-from-motion’photogrammetry: A low-cost, effective tool for geoscience applications. *Ge-*
577 *omorphology*, 179:300–314, 2012.

578 Enze Xie, Wenhai Wang, Zhiding Yu, Anima Anandkumar, Jose M Alvarez, and Ping Luo. Segformer:
579 Simple and efficient design for semantic segmentation with transformers. *Adv. Neural Inform. Pro-*
580 *cess. Syst.*, 34:12077–12090, 2021.

581 Yuhui Yuan and Jingdong Wang. Ocnet: Object context network for scene parsing. *arXiv preprint*
582 *arXiv:1809.00916*, 2018.

583 Yuhui Yuan, Xilin Chen, and Jingdong Wang. Object-contextual representations for semantic segmen-
584 tation. In *Eur. Conf. Comput. Vis.*, pages 173–190. Springer, 2020.

585 Zhen Zhang, Yang Zhou, Haiyun Liu, and Hongmin Gao. In-situ water level measurement using
586 nir-imaging video camera. *Flow Measurement and Instrumentation*, 67:95–106, 2019.

587 Hengshuang Zhao, Jianping Shi, Xiaojuan Qi, Xiaogang Wang, and Jiaya Jia. Pyramid scene parsing
588 network. In *Proceedings of the IEEE conference on computer vision and pattern recognition*, pages
589 2881–2890, 2017.

590 Yufeng Zheng, Jun Huang, Tianwen Chen, Yang Ou, and Wu Zhou. Processing global and local features
591 in convolutional neural network (cnn) and primate visual systems. In *Mobile Multimedia/Image*
592 *Processing, Security, and Applications 2018*, volume 10668, pages 44–51. SPIE, 2018.

593 Zhen Zhu, Mengde Xu, Song Bai, Tengting Huang, and Xiang Bai. Asymmetric non-local neural
594 networks for semantic segmentation. In *Int. Conf. Comput. Vis.*, pages 593–602, 2019.

EYE OF HORUS: A VISION-BASED FRAMEWORK FOR REAL-TIME WATER LEVEL MEASUREMENT

Mohammad H. Erfani¹, Corinne Smith², Zhenyao Wu³, Elyas Asadi Shamsabadi⁴, Farboud Khatami¹, Austin R.J. Downey^{1,2}, Jasim Imran¹, and Erfan Goharian^{*1}

¹Department of Civil & Environmental Engineering, University of South Carolina Columbia, SC 29208, USA

²Department of Mechanical Engineering, University of South Carolina, Columbia, SC 29208, USA

³Department of Computer Science & Engineering, University of South Carolina, Columbia, SC 29201, USA

⁴School of Civil Engineering, Faculty of Engineering, The University of Sydney, Sydney, NSW 2006, Australia

Abstract

Heavy rains and tropical storms often result in floods, which are expected to increase in frequency and intensity. Flood prediction models and inundation mapping tools provide decision-makers and emergency responders with crucial information to better prepare for these events. However, the performance of models relies on the accuracy and timeliness of data received from in-situ gaging stations and remote sensing; each of these data sources has its limitations, especially when it comes to real-time monitoring of floods. This study presents a vision-based framework for measuring water levels and detecting floods using Computer Vision and Deep Learning (DL) techniques. The DL models use time-lapse images captured by surveillance cameras during storm events for the semantic segmentation of water extent in images. Three different DL-based approaches, namely PSPNet, TransUNet, and SegFormer, were applied and evaluated for semantic segmentation. The predicted masks are transformed into water level values by intersecting the extracted water edges, with the 2D representation of a point cloud generated by an Apple iPhone 13 Pro LiDAR sensor. The estimated water levels were compared to reference data collected by an ultrasonic sensor. The results showed that SegFormer outperformed other DL-based approaches by achieving 99.55% and 99.81% for Intersection over Union (IoU) and accuracy, respectively. Moreover, the highest correlations between reference data and the vision-based approach reached above 0.98 for both the coefficient of determination (R^2) and Nash-Sutcliffe Efficiency. This study demonstrates the potential of using surveillance cameras and Artificial Intelligence for hydrologic monitoring and their integration with existing surveillance infrastructure.

1 Introduction

Flood forecasts and Flood Inundation Mapping (FIM) can play an important role in saving human lives and reducing damages by providing timely information for evacuation planning, emergency management, and relief efforts [Gebrehiwot et al., 2019]. These models and tools are designed to identify and predict inundation areas and the severity of damage caused by storm events. Two primary sources of data for these models are in-situ gaging networks and remote sensing. For example, in-situ stream gages, such as those operated by the United States Geological Survey (USGS) provide useful stream-flow information like water height and discharge at monitoring sites [Turnipseed and Sauer, 2010]. However, they cannot provide an adequate spatial resolution of streamflow characteristics [Lo et al., 2015]. The limitation of in-situ stream gages is further exacerbated by the lack of systematic installation along the waterways and accessibility issues [Li et al., 2018; King et al., 2018]. Satellite data and remote sensing can complement in-situ gage data by providing information at a larger spatial scale [Alsdorf et al., 2007]. However, continuous monitoring data for a region of interest remains to be a problem due to the limited revisit intervals of satellites, cloud cover, and systematic departures or biases [Panteras and Cervone, 2018]. Crowdsourcing methods have gained attention as a potential solution but their reliability is questionable [Schnebele et al., 2014; Goodchild, 2007; Howe, 2008]. To address these limitations and enhance real-time monitoring capabilities, surveillance cameras are inves-

*goharian@cec.sc.edu

46 tigated here as a new source of data for hydrologic monitoring and flood data collection. However, this
47 requires a significant investment in Computer Vision (CV) and Artificial Intelligence (AI) techniques
48 to develop reliable methods for detecting water in surveillance images and translating that information
49 into numerical data.

50 Recent advances in CV offer new techniques for processing image data for the quantitative measure-
51 ments of physical attributes from a site [Forsyth and Ponce, 2002]. However, there is limited knowledge
52 of how visual information can be used to estimate physical water parameters using CV techniques.
53 Inspired by the principle of the float method, Tsubaki et al. [2011] used different image processing tech-
54 niques to analyze images captured by closed-circuit television (CCTV) systems installed for surveillance
55 purposes to measure the flow rate during flood events. In another example, Kim et al. [2011] proposed
56 a method for measuring water level by detecting the borderline between a staff gauge and the surface
57 of water based on image processing of the captured image of the staff gage installed in the middle of
58 the river. As the use of images for environmental monitoring becomes more popular, several studies
59 have investigated the source and magnitude of errors common in image-based measurement systems,
60 such as the effect of image resolution, lighting effects, perspective, lens distortion, water meniscus,
61 and temperature changes [Elias et al., 2020; Gilmore et al., 2013]. Furthermore, proposed solutions
62 to resolve difficulties originating from poor visibility have been developed to better identify readings
63 on staff gages [Zhang et al., 2019]. Recently, Deep Learning (DL) has become prevalent across a wide
64 range of disciplines, particularly in applied sciences such as CV and engineering.

65 DL-based models have been utilized by the water resources community to determine the extent of water
66 and waterbodies visible in images captured by surveillance camera systems. These models can estimate
67 the water level [Pally and Samadi, 2022]. In a similar vein, Moy de Vitry et al. [2019] employed a DL-
68 based approach to identify floodwater in surveillance footage and introduced a novel qualitative flood
69 index, SOFI, to determine water level fluctuations. SOFI was calculated by taking the aspect ratio of
70 the area of the water surface detected within an image to the total area of the image. However, these
71 types of methods, which make prior assumptions and estimate water level fluctuation roughly, cannot
72 serve as a vision-based alternative for measuring streamflow characteristics. More systematic studies
73 adopted photogrammetry to reconstruct a high-quality 3D model of the environment with a high
74 spatial resolution to have a precise estimation of real-world coordination while measuring streamflow
75 rate and stage. For example, Eltner et al. [2018, 2021] introduced a method based on Structure
76 from Motion (SfM), and photogrammetric techniques, to automatically measure the water stage using
77 low-cost camera setups.

78 Advances in photogrammetry techniques enable 3D surface reconstruction with a high temporal and
79 spatial resolution. These techniques are adopted to build 3D surface models from RGB imagery [West-
80 oby et al., 2012; Eltner and Schneider, 2015; Eltner et al., 2016]. However, most of the photogrammetric
81 methods are still expensive as they rely on differential global navigation satellite systems (DGNSS),
82 ground control points (GCPs), commercial software, and data processing on an external computing
83 device [Froideval et al., 2019]. A LiDAR scanner, on the other hand, is now easily available since the
84 introduction of the iPad Pro and iPhone 12 Pro in 2020 by Apple. This device is the first smartphone
85 equipped with a native LiDAR scanner and offers a potential paradigm shift in digital field data acqui-
86 sition which puts these devices at the forefront of smartphone-assisted fieldwork [Tavani et al., 2022].
87 So far, the iPhone LiDAR sensor has been used in different studies such as forest inventories [Gollob
88 et al., 2021] and coastal cliff site [Luetzenburg et al., 2021]. The availability of LiDAR sensors to build
89 3D environments, and advancements in DL-based models offer a great potential to produce numerical
90 information from ground-based imageries.

91 This paper presents a vision-based framework for measuring water levels from time-lapse images. The
92 proposed framework introduces a novel approach by utilizing the iPhone LiDAR sensor as a laser scan-
93 ner, which is commonly available on consumer-grade devices, for scanning and constructing a 3D point
94 cloud of the region of interest. During the data collection phase, time-lapse images and ground truth
95 water level values were collected using an embedded camera and ultrasonic sensor. The water extent
96 in the captured images was determined automatically using semantic segmentation DL-based models.
97 For the first time, the performance of three different state-of-the-art DL-based approaches, including
98 Convolutional Neural Networks (CNN), hybrid CNN-Transformer, and Transformers-Multilayer Per-
99 ceptron (MLP), was evaluated and compared. CV techniques were applied for camera calibration, pose

100 estimation of the camera setup in each deployment, and 3D-2D reprojection of the point cloud onto
101 the image plane. Finally, K-Nearest Neighbors (KNN) was used to find the nearest projected (2D)
102 point cloud coordinates to the water line on the river banks, for estimating the water level in each
103 time-lapse image.

104 2 Deep Learning Architectures

105 Since this study tends to cover a wide range of DL approaches, this section solely focuses on reviewing
106 different DL-based architectures. So far, different DL networks were applied and evaluated for semantic
107 segmentation of the waterbodies within the RGB images captured by cameras [Erfani et al., 2022]. All
108 existing semantic segmentation approaches—CNN and Transformer-based—share the same objective of
109 classifying each pixel of a given image but differ in the network design.

110 CNN-based models were designed to imitate the recognition system of primates [Shamsabadi et al.,
111 2022], while possessing different network designs such as low-resolution representations learning [Long
112 et al., 2015; Chen et al., 2017], high-resolution representations recovering [Badrinarayanan et al., 2015;
113 Noh et al., 2015; Lin et al., 2017], contextual aggregation schemes [Yuan and Wang, 2018; Zhao et al.,
114 2017; Yuan et al., 2020], feature fusion and refinement strategy [Lin et al., 2017; Huang et al., 2019;
115 Li et al., 2019; Zhu et al., 2019; Fu et al., 2019]. CNN-based models follow local to global features in
116 different layers of the forward pass, which used to be thought of as a general intuition of the human
117 recognition system. In this system, objects are recognized through the analysis of texture and shape-
118 based clues—local and global representations and their relationship in the entire field of view. Recent
119 research, however, shows significant differences exist between the visual behavioral system of humans
120 and CNN-based models [Geirhos et al., 2018b; Dodge and Karam, 2017; De Cesarei et al., 2021; Geirhos
121 et al., 2020, 2018a], and reveal higher sensitivity of the visual systems in humans to global features
122 rather than local ones [Zheng et al., 2018]. This fact drew attention to models that focus on the global
123 context in their architectures.

124 Developed by Dosovitskiy et al. [2020], Vision Transformer (ViT) was the first model that showed
125 promising results on a computer vision task (image classification) without using convolution operation
126 in its architecture. In fact, ViT adopts “Transformers,” as a self-attention mechanism, to improve
127 accuracy. “Transformer” was initially introduced for sequence-to-sequence tasks such as text trans-
128 lation [Vaswani et al., 2017]. However, as applying the self-attention mechanism on all image pixels
129 is computationally expensive, the Transformer-based models could not compete with the CNN-based
130 models until the introduction of ViT architecture which applies self-attention calculations on the low-
131 dimension embedding of small patches originating from splitting the input image, to extract global
132 contextual information. Successful performance of ViT on image classification inspired several subse-
133 quent works on Transformer-based models for different computer vision tasks [Liu et al., 2021].

134 In this study, three different DL-based approaches including CNN, hybrid CNN-Transformer, and
135 Transformers-Multilayer Perceptron (MLP) were trained and tested for semantic segmentation of wa-
136 ter. For these approaches, the selected models were PSPNet [Zhao et al., 2017], TransUNet [Chen
137 et al., 2021] and SegFormer [Xie et al., 2021], respectively. The performance of these models is evalu-
138 ated and compared using conventional metrics, including class-wise Intersection over Union (IoU) and
139 per-pixel accuracy (ACC).

140 3 Study Area

141 In order to evaluate the performance of the proposed framework for measuring the water levels in rivers
142 and channels, a time-lapse camera system has been deployed at Rocky Branch, South Carolina. This
143 creek is approximately 6.5 km long and collects stormwater from the University of South Carolina
144 campus and the City of Columbia. Rocky Branch is subjected to rapid changes in water flow and
145 discharges into the Congaree River [Morsy et al., 2016]. The observation site is located within the
146 University of South Carolina campus behind 300 Main Street. An Apple iPhone 13 Pro LiDAR sensor
147 was used to scan the region of interest (see Figure 1a). Although there is no official information about
148 the technology and hardware specifications, Gollob et al. [2021] reports the LiDAR module operates
149 at the 8XX nm wavelength and consists of an emitter (Vertical Cavity Surface-Emitting Laser with

150 Diffraction Optics Element, VCSEL DOE) and a receptor (Single Photon Avalanche Diode array-
151 based Near Infrared Complementary Metal Oxide Semiconductor image sensor, SPAD NIR CMOS)
152 based on direct-time-of-flight technology. Comparisons between the Apple LiDAR sensor and other
153 types of laser scanners including hand-held, industrial, and terrestrial have been conducted by several
154 recent studies [Mokroš et al., 2021; Vogt et al., 2021]. Gollob et al. [2021] tested and reported the
155 performance of a set of eight different scanning apps, and found three applications including 3D
156 Scanner App, Polycam and SiteScape suitable for actual practice tests. The objective of this study
157 is not the evaluation of the iPhone LiDAR sensor and app performance. Therefore, the 3D Scanner
158 App [LABS, 2022] was used with the following settings: confidence = high, range = 5.0 m, masking =
159 none, and resolution = 5 mm, for scanning and 3D reconstruction processing. The scanned 3D point
160 cloud is shown in Figure 1b.

161 As the LiDAR scanner settings were set at the highest level of accuracy and computational demand,
162 scanning the whole region of interest at the same time was not possible. So, the experimental region
163 was divided into several sub-regions and scanned in multi-step. In order to assemble the sub-region
164 LiDAR scans, several GCPs were considered in the study area. These GCPs were measured by a
165 total station (Topcon GM Series). Moreover, 13 Aruco markers were installed for estimating extrinsic
166 camera parameters in each setup deployment. Since it was not possible to accurately measure the real-
167 world coordination of Aruco markers by the LiDAR scanner, the coordinates of the top-left corner
168 of markers were also measured by the surveying total station. The 3D point cloud scanned for each
169 sub-region was transformed into the total station coordinate system, and the real-world coordinates of
170 ArUco markers were appended to the 3D point cloud for the following analyses.

171 4 Methodology

172 This study introduces the Eye of Horus, a vision-based framework for hydrologic monitoring and
173 real-time water level measurements in bodies of water. The proposed framework includes three main
174 components. The first step is designing two deployable setups for data collection. These setups consist
175 of a programmable time-lapse camera run by Raspberry Pi and an ultrasonic sensor run by Arduino.
176 After collecting data, the first phase (Module 1) involves configuring and training DL-based models
177 for semantic segmentation of water in the captured images. In the second phase (Module 2), CV
178 techniques for camera calibration, spatial resection, and calculating projection matrix are discussed.
179 Finally, in the third phase (Module 3), an ML-based model uses the information achieved by CV
180 models to find the relationships between real-world coordinates of water level in the captured images
181 (see Figure 2).

182 4.1 Data Acquisition

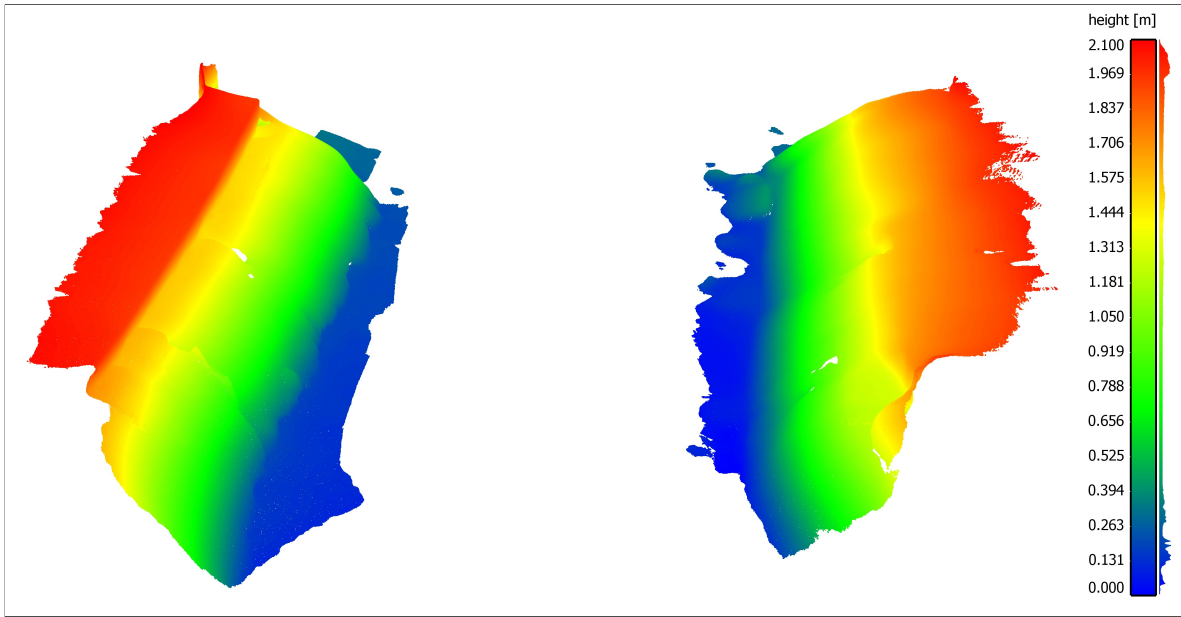
183 Two different single-board computers (SBC) were used in this study, Raspberry Pi (Zero W) for
184 capturing time-lapse images of a river scene, and Arduino (Nano 3.x) for measuring water level as the
185 ground truth data. These devices were designed to communicate with each other, i.e., to trigger the
186 other to start or stop recording. During capturing time-lapse images, the Pi camera device triggers the
187 ultrasonic sensor for measuring the corresponding water level. The camera device is equipped with the
188 Raspberry Pi Camera Module 2 which has a Sony IMX219 8-megapixel sensor. This sensor is able to
189 capture an image size of $4,256 \times 2,832$ pixels. However, in this study, the image resolution was set to
190 $1,920 \times 1,440$ pixels to balance image quality and computational cost in subsequent image processing
191 steps. This setup is also equipped with a 1200 mAh UPS lithium battery power module to provide
192 uninterrupted power to the Pi SBC (see Figure 3a).

193 The Arduino-based device records the water level. The design is based on an unmanned aerial ve-
194 hicle (UAV) deployable sensor created by Smith et al. [2022]. The nRF24L01+ single-chip 2.4 GHz
195 transceiver allows the Arduino and Raspberry Pi to communicate via radio frequency (RF). The chip
196 is housed in both packages and the channel, pipe addresses, data rate, and transceiver/receiver con-
197 figuration are all set in the software. The HC-SR04 ultrasonic sensor is mounted to the base of the
198 Arduino device and provides a contactless water level measurement. Two permanent magnets at the
199 top of the housing attach to a ferrous structure and allow the ultrasonic sensor to be suspended up to
200 14 feet over the surface of the water. The device also includes a microSD card module and DS3231



(a)

(b)



(c)

Figure 1: Study area of the Rocky Branch Creek. (a) View of the region of interest, (b) The scanned 3D point cloud of the region of interest including an indication of the ArUco markers' locations, and (c) The scalar field of left and right banks of Rocky Branch in the region of interest (the colorbar and the frequency distribution of z values for the captured points are shown on the right side).

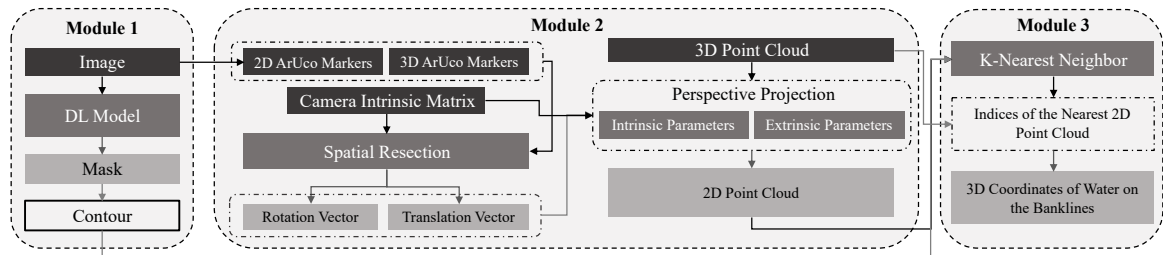


Figure 2: The Eye of Horus workflow includes three main modules starting from processing images captured by the time-lapse camera to estimating water level by projecting the waterline on river banks using CV techniques.

201 real-time clock, which enable data logging and storage on-device as well as transmission. The device
 202 is powered by a rechargeable 7.4V 1500 mAh lithium polymer battery (see Figure 3b).

203 The Arduino device waits to receive a ping from the Raspberry Pi device to initiate data collection.
 204 The ultrasonic sensor measures the distance from the sensor transducer to the surface of the water.
 205 The nRF24L01+ transmits this distance to the Raspberry Pi device and saves the measurement and a
 206 time stamp from the real-time clock to an onboard microSD card. This acts as backup data storage, in
 207 case transmission to the Raspberry Pi fails. The nRF24L01+ RF transceivers have an experimentally
 208 determined range of up to 30 ft which allows flexibility in the relative placement of the camera to the
 209 measuring site.

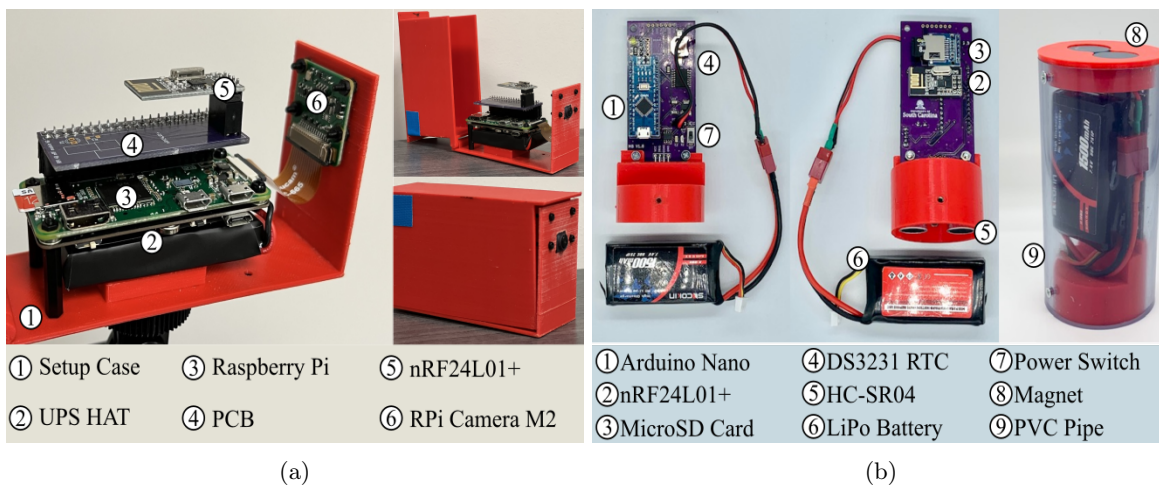


Figure 3: Data acquisition devices. (a) Beena, run by Raspberry Pi (Zero W) for capturing time-lapse images of the river scene; and (b) Aava, run by Arduino Nano for measuring water level correspondence.

210 A dataset for semantic segmentation was created by collecting images from a specific region of interest
 211 at different times of the day and under various flow regimes. This dataset includes 1,172 images, with
 212 manual annotations of the streamflow in the creek for all of them. The dataset is further divided into
 213 812 training images, 124 validation images, and 236 testing images.

214 4.2 Deep Learning Model for Water Segmentation

215 The water extent can be automatically determined on the 2D image plane with the help of DL-based
 216 models. The task of semantic segmentation was applied within the framework of this study to delineate
 217 the water line on the left and right banks of the channel. Three different DL-based models were trained
 218 and tested in this study. PSPNet, the first model, is a CNN-based semantic segmentation multi-scale
 219 network which can better learn the global context representation of a scene [Zhao et al., 2017]. ResNet-
 220 101 [He et al., 2016] was used as the backbone of this model to encode input images into the features.
 221 ResNet architecture takes the advantage of “Residual blocks” that assist the flow of gradients during
 222 the training stage allowing effective training of deep models even up to hundreds of layers. These
 223 extracted features are then fed into a pyramid pooling module in which feature maps produced by
 224 small to large kernels are concatenated to distinguish patterns of different scales [Minaee et al., 2021].

225 TransUNet, the second model, is a U-shaped architecture that employs a hybrid of CNN and Trans-
 226 formers as the encoder to leverage both the local and global contexts for precise localization and
 227 pixel-wise classification [Chen et al., 2021]. In the encoder part of the network, CNN is first used as a
 228 feature extractor to generate a feature map for the input image, which is then fed into Transformers
 229 to extract long-range dependencies. The resulting features are upsampled in the decoding path and
 230 combined with detailed high-resolution spatial information skipped from the CNN to make estimations
 231 on each pixel of the input image.

232 SegFormer, the third model, unifies a novel hierarchical Transformer, which does not require the posi-
 233 tional encodings used in standard Transformers, and MultiLayer Perceptron (MLP) performs efficient

segmentation [Xie et al., 2021]. The hierarchical Transformer introduced in the encoder of this architecture gives the model the attention ability to multiscale features (high-resolution fine and low-resolution coarse information) in the spatial input without the need for positional encodings that may adversely affect a models performance when testing on a different resolution from training. Moreover, unlike other segmentation models that typically use deconvolutions in the decoder path, a lightweight MLP is employed as the decoder of this network that inputs the features extracted at different stages of the encoder to generate a prediction map faster and more efficiently. Two different variants, including SegFormer-B0 and SegFormer-B5, were applied in this study. The configuration of the models implemented in this study is elaborated in Table 1. The total number of parameters (Params), occupied memory size on GPU (Total Size), and input image size (Batch Size) are reported in Million (M), Megabyte (MB), and Batch size \times Height \times Width \times Channel (B, H, W, C) respectively.

Table 1: The configuration of models trained and tested in this study.

Model Names	Params (M)	Total Size (MB)	Batch Size (B, H, W, C)	Loss Function	Optimizer	LR
PSPNet	66.2	7,178	$2\times 500\times 500\times 3$	Binary Cross Entropy	SGD	2.50E-04
TransUNet	20.1	6,017	$2\times 448\times 448\times 3$	Cross Entropy + Dice	SGD	2.50E-04
SegFormer-B0	3.7	2,217	$2\times 512\times 512\times 3$	Cross Entropy	AdamW	6.00E-05
SegFormer-B5	82.0	27,666	$2\times 1024\times 1024\times 3$	Cross Entropy	AdamW	6.00E-05

The models were implemented using PyTorch. During the training procedure, the loss function, optimizer, and learning rate were set individually for each model based on the results of preliminary runs used to find the optimal hyperparameters. In the case of PSPNet and TransUNet, the base learning rate was set to 2.5×10^{-4} and decayed using the poly policy [Zhao et al., 2017]. These networks were optimized using stochastic gradient descent (SGD) with a momentum of 0.9 and weight decay of 0.0001. For SegFormer (B0 and B5), a constant learning rate of 6.0×10^{-5} was used, and the networks were trained with the AdamW optimizer [Loshchilov and Hutter, 2017]. All networks were trained for 30 epochs with a batch size of two. The training data for PSPNet and TransUNet were augmented with horizontal flipping, random scaling, and random cropping.

4.3 Projective Geometry

In this study, CV techniques are used for different purposes. First, CV models were used for camera calibration. They include focal length, optical center, radial distortion, camera rotation, and translation. These parameters provide the information (parameters or coefficients) about the camera that is required to determine the relationship between 3D object points in the real-world coordinate system and its corresponding 2D projection (pixel) in the image captured by that calibrated camera. Generally, camera calibration models estimate two kinds of parameters. First, the internal parameters of the camera (e.g., focal length, optical center, and radial distortion coefficients of the lens). Second, external parameters (refer to the orientation– rotation and translation– of the camera with respect to the real-world coordinate system.

To estimate the camera intrinsic parameters, OpenCV built-in was applied for camera calibration using a 2D checkerboard [Bradski, 2000]. Intrinsic parameters are specific to a camera. The focal length (f_x, f_y) and optical centers (c_x, c_y) can be used to create a camera matrix. The camera matrix is unique to a specific camera, so once calculated, it can be reused on other images taken by the same camera (Equation 1). It is expressed as a 3×3 matrix:

$$\text{camrea matrix} = \begin{bmatrix} f_x & 0 & c_x \\ 0 & f_y & c_y \\ 0 & 0 & 1 \end{bmatrix} \quad (1)$$

The camera extrinsic parameters were determined using the pose estimation problem which consists in solving for the rotation, and translation that minimizes the reprojection error from 2D-3D point correspondences [Marchand et al., 2015]. For this purpose, the iterative method was applied which is based on a Levenberg-Marquardt optimization. In this task the function finds such a pose that

273 minimizes reprojection error, that is the sum of squared distances between the observed projections
 274 “image point” and the projected “object points.” The initial solution for non-planar 3D object points
 275 needs at least six points and uses the Direct Linear Transformation (DLT) algorithm.

$$\begin{bmatrix} u \\ v \\ 1 \end{bmatrix} = \underbrace{\begin{bmatrix} f_x & 0 & c_x & 0 \\ 0 & f_y & c_y & 0 \\ 0 & 0 & 1 & 0 \end{bmatrix}}_{\mathbf{K}} \underbrace{\begin{bmatrix} r_{11} & r_{12} & r_{13} & t_x \\ r_{21} & r_{22} & r_{23} & t_y \\ r_{31} & r_{32} & r_{33} & t_z \\ 0 & 0 & 0 & 1 \end{bmatrix}}_{[\mathbf{R}|\mathbf{t}]} \begin{bmatrix} X_w \\ Y_w \\ Z_w \\ 1 \end{bmatrix} \quad (2)$$

276 Equation 2 represents “Projection Matrix” consisting of two parts– the intrinsic matrix (\mathbf{K}) that
 277 contains the intrinsic parameters and the extrinsic matrix ($[\mathbf{R} \mid \mathbf{t}]$) that is a combination of 3×3
 278 rotation matrix \mathbf{R} and a 3×1 translation \mathbf{t} vector.

279 2D points are represented with ArUco markers’ pixel coordinates on the 2D image plane, and cor-
 280 responding 3D object points are measured by the total station. Having at least six 3D-2D point
 281 correspondences, the spatial position and orientation of the camera can be estimated for each setup
 282 deployment. After retrieving all the necessary parameters, a full-perspective camera model can be
 283 generated. Using this model, the 3D point cloud is projected on the 2D image plane. The projected
 284 (2D) point cloud can represent 3D real-world coordinates of the nearest 2D pixel correspondence on
 285 the image plane.

286 4.4 Machine Learning for Image Measurements

287 Using the projection matrix, the 3D point cloud is projected on the 2D image plane (see Figure 4). The
 288 projected (2D) point cloud is intersected with the water line pixels, the output of the DL-based model
 289 (Module 1), to find the nearest point cloud coordinate. To achieve this objective, we utilize the K-
 290 Nearest Neighbors (KNN) algorithm. Notably, the indices of the selected points remain consistent for
 291 both the 3D point cloud and the projected (2D) correspondences. As a result, by utilizing the indices
 292 of the chosen projected (2D) points, the corresponding real-world 3D coordinates can be retrieved.

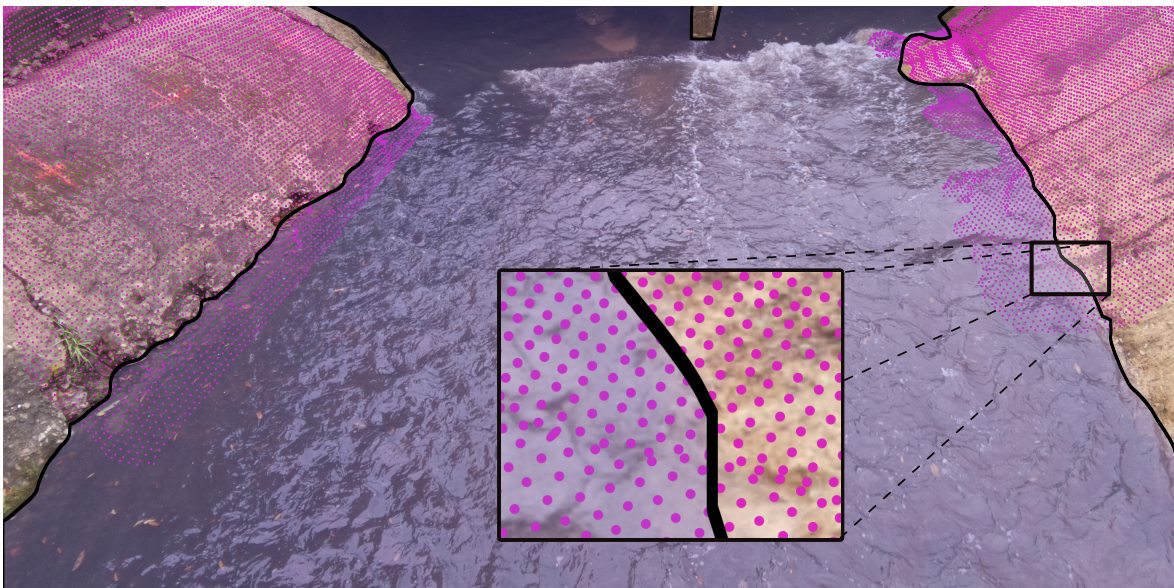


Figure 4: KNN is used to find the nearest projected (2D) point cloud (magenta dots) to the water line (black line) on the image plane.

5 Results and Discussion

The results of this study are presented in two sections. First, the performance of DL-based models is discussed. Then, in the second section, the performance of the proposed framework is evaluated for five different deployments.

5.1 DL-based Models Results

The performance of DL-based models for the task of semantic segmentation is evaluated and compared in this section. Since the proposed dataset includes just two classes, “river” and “non-river”, “non-river” was omitted from the evaluation process, and the performance of models is only reported for the “river” class of the test set. The class-wise intersection over union (IoU) and the per-pixel accuracy (ACC) were considered the main evaluation metrics in this study. According to Table 2, both variants of SegFormer— SegFormer-B0, and SegFormer-B5— outperform other semantic segmentation networks on the test set. Considering the models’ configurations detailed in Table 1, SegFormer-B0 can be considered the most efficient DL-based network, as it is comprised of only 3.7 M trainable parameters and occupies just 2,217 Megabytes of GPU ram during training. In Figure 5, four different visual representations of the models’ performance on the validation set of the proposed dataset are presented. Since the water level is estimated by intersecting the water line on river banks with the projected (2D) point cloud, precise delineation of the water line is of utmost importance to achieve better results in the following steps. This means that estimating the correct location of the water line on creek banks in each time-lapse image plays a more significant role than performance metrics in this study. Taking the quality of water line detection into account and based on the visual representations shown in Figure 5, SegFormers’ variants still outperform DL-based approaches. In this regard, a comparison of PSPNet and TransUNet showed that PSPNet can delineate the water line more clearly, while the segmented area is more integrated for TransUNet outputs.

Table 2: The performance metrics of different DL-based approaches.

Model Names	IoU (River)	ACC (River)
PSPNet	94.88%	95.84%
TransUNet	93.54%	96.89%
SegFormer-B0	99.38%	99.77%
SegFormer-B5	99.55%	99.81%

CNNs are typically limited by the nature of their convolution operations, leading to architecture-specific issues such as locality [Geirhos et al., 2018a]. Consequently, CNN-based models may achieve high accuracy on training data, but their performance can decrease considerably on unseen data. Additionally, compared to Transformer-based networks, they perform poorly at detecting semantics that requires combining long- and short-range dependencies. Transformers can relax the biases of DL-based models inducted by Convolutional operations, achieving higher accuracy in localization of target semantics and pixel-level classification with lower fluctuations in varied situations through the leverage of both local and global cues [Naseer et al., 2021]. Yet, various transformer-based networks may perform differently depending on the targeted task and the network’s architecture. TransUNet adopts Transformers as part of its backbone; however, Transformers generate single-scale low-resolution features as output [Xie et al., 2021], which may limit the accuracy when multi-scale objects or single objects with multi-scale features are segmented. The problem of producing single-scale features in standard Transformers is addressed in SegFormer variants through the use of a novel hierarchical Transformer encoder [Xie et al., 2021]. This approach has resulted in human-level accuracy being achieved by Segformer-B0 and -B5 in the delineation of the water line, as shown in Figure 5. The predicted masks are in satisfactory agreement with the manually annotated images.

5.2 Water Level Estimation

This section reports the framework performance based on several deployments in the field. The performance results are separately shown for the left and right banks and compared with ultrasonic sensor data as the ground truth. The ultrasonic sensor was evaluated previously that documented an average

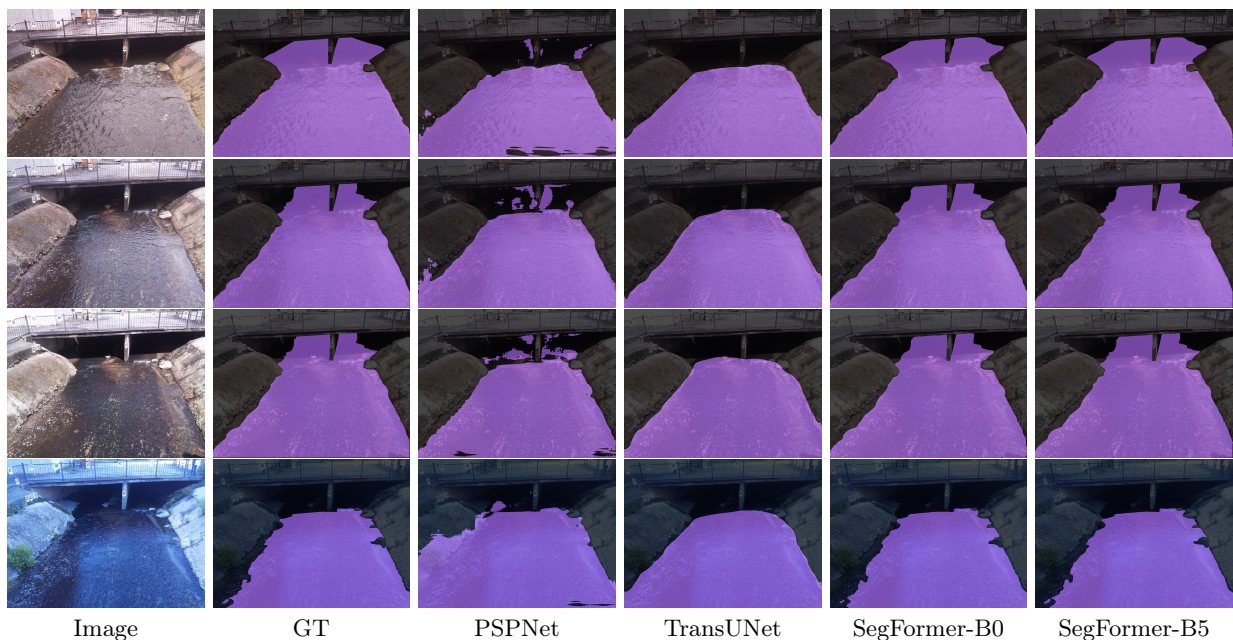


Figure 5: Visual representations of different DL-based image segmentation approaches on the validation dataset.

336 distance error of 6.9 mm [Smith et al., 2022]. Four different efficiency criteria including coefficient of
 337 determination (R^2), Nash-Sutcliffe Efficiency (NSE), Root Mean Square Error (RMSE), and Percent
 338 bias (PBIAS) are reported in Table 3. R^2 , as the most representative metric, emphasizes how much
 339 of the observed dispersion can be explained by the prediction. However, if the model systematically
 340 over- or under-estimates the results, R^2 will still be close to 1.0 as it only takes dispersion into ac-
 341 count [Krause et al., 2005]. NSE, a traditional metric used in hydrology is also used to summarize model
 342 performance. NSE normalizes model performance into an interpretable scale and is commonly used to
 343 differentiate between ‘good’ and ‘bad’ models [Knoben et al., 2019]. RMSE represents the square root
 344 of the average of squares of the errors, the differences between predicted values and observed values.
 345 The PBIAS of estimated water level, compared against the ultrasonic sensor data was also used to
 346 show where the two estimates are close to each other and where they significantly diverge [Lin et al.,
 347 2020].

Table 3: The performance metrics of the framework for five different days of setup deployment.

Deployment Date	Position	Metrics			
		R^2	NSE	RMSE	PBIAS
Aug/17/2022	Left Bankline	0.8019	0.5258	0.0409	10.6401
	Right Bankline	0.7932	0.7541	0.0294	-0.4848
Aug/19/2022	Left Bankline	0.7701	0.5713	0.0647	16.1015
	Right Bankline	0.9678	0.9588	0.0201	-3.4752
Aug/25/2022	Left Bankline	0.7690	0.5700	0.0435	-7.7091
	Right Bankline	0.8922	0.8711	0.0238	-1.7738
Nov/10/2022	Left Bankline	0.9461	0.8129	0.0511	-13.1183
	Right Bankline	0.9857	0.9790	0.0171	-1.5210
Nov/11/2022	Left Bankline	0.9588	0.8881	0.0397	-10.3656
	Right Bankline	0.9855	0.9829	0.0155	-1.7987

348 The setup was deployed on several rainy days. In addition to Table 3, the results of each deployment are
 349 visually demonstrated in Figure 6. The scatter plots show the relationships between the ground truth
 350 data (measured by the ultrasonic sensor), and the banks of the river. The scatter plots visually present

351 whether the camera readings overestimate or underestimate the ground truth data. Moreover, the time-
352 series plot of water level is shown for each deployment separately. A hydrograph, showing changes in
353 the water level of a stream over time can be a useful tool for demonstrating whether camera readings
354 can satisfactorily capture the response of a catchment area to rainfall. The proposed framework can
355 be evaluated in terms of its ability to accurately track and identify important characteristics of a flood
356 wave, such as the rising limb, peak, and recession limb.

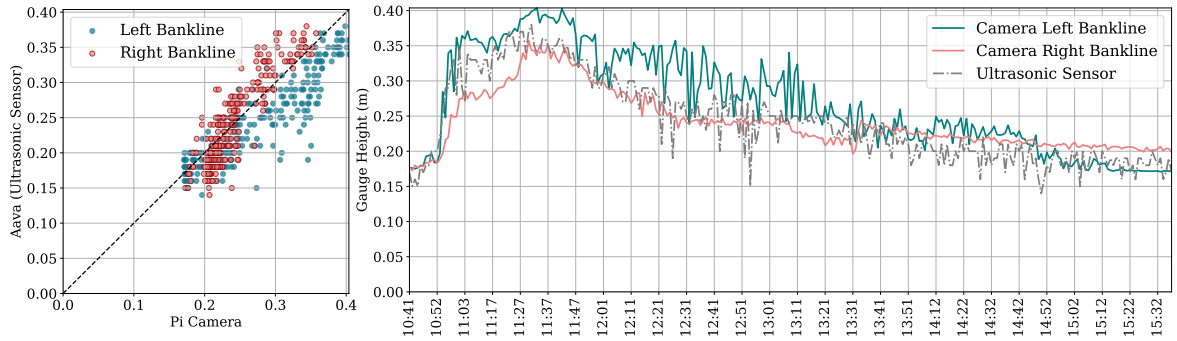
357 The first deployment was done on Aug 17, 2022 (see Figure 6a). The initial water level of the base
358 flow and parts of the rising limb were not captured in this deployment. Table 3 shows that the
359 performance results of the right bank camera readings are better than those of the left bank. R^2 for
360 both banks was about 0.80 showing a strongly related correlation between the water level estimated by
361 the framework and ground truth data. Figure 6a shows how the left and right bank camera readings
362 perform during the rising limb; the right bank camera readings still underestimated the water level
363 during this time frame, and during the recession limb, the left bank camera readings overestimated
364 the water level. However, the hydrograph plot shows that both left and right bank camera readings
365 were able to capture the peak water level.

366 The second deployment was done on Aug 19, 2022. In this deployment, all segments of the hydrograph
367 were captured. According to Table 3, the performance of the right bank camera readings was better
368 than the left bank one; more than 0.95 was reported for R^2 and NSE of the right bankline. Figure 6b
369 shows during the rising limb and crest segment both banks estimated the water level similar to ground
370 truth. During the recession limb, the right bank water level estimation kept coincident with ground
371 truth, while the left bank overestimated the water level. The third deployment was on Aug 25, 2022.
372 This time water level of the recession limb and the following base flow were captured (see Figure 6c).
373 The right bank camera readings with R^2 of 0.89 performed better than the left bank. This time, left
374 bank camera readings underestimated the water level over the recession limb, but during the following
375 base flow, the water level was estimated correctly by cameras on both banks.

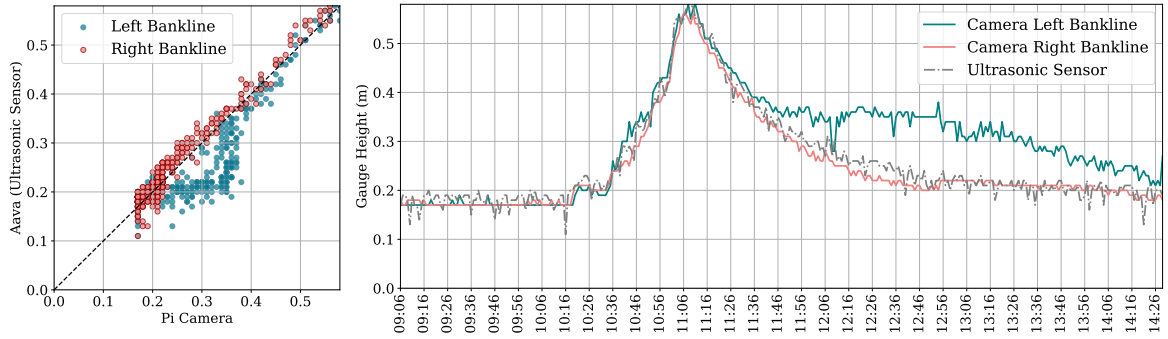
376 The results indicate that the right bank camera readings performed better than the left bank. Further
377 investigation of the field conditions revealed that stream erosion had a more significant impact on the
378 concrete surface of the left bank, resulting in patches and holes that were not scanned by the iPhone
379 LiDAR. As a result, the KNN algorithm used to find the nearest (2D) point cloud coordinates to the
380 water line could not accurately represent the corresponding real-world coordinates of these locations.
381 Figure 7 shows a box plot and scatter plot of the estimated water level for a time-lapse image captured
382 at 13:29 on Aug 19, 2022. The patches and holes on the left bank surface caused instability in water
383 level estimation for the region of interest. The box plot of the left bank (Cam-L-BL) was taller than
384 that of the right bank (Cam-R-BL), indicating that the estimated water level was spread over larger
385 values in the left bank due to the presence of these irregularities.

386 After analyzing the initial results, the deployable setups were modified to enhance the quality of data
387 collection. The programming code of the Arduino device, Aava, was modified to measure five different
388 records for water level, each time it is triggered by the camera device, Beena, and transmit the average
389 distance to the Raspberry Pi device. This modification decreased the number of noise spikes in the
390 measured data and allowed a better comparison between camera readings and ground truth data.
391 The case of the camera device, Beena, was redesigned to protect the single board against rain without
392 requiring an umbrella which makes the camera setup unstable in stormy weather and causes a decrease
393 in the precision of measurements. Moreover, an opening is incorporated into the redesigned case to
394 connect an external power bank to enhance the run time. Finally, the viewpoint of the camera was
395 subtly shifted to the right to adjust the share of the river banks on the camera's field of view.

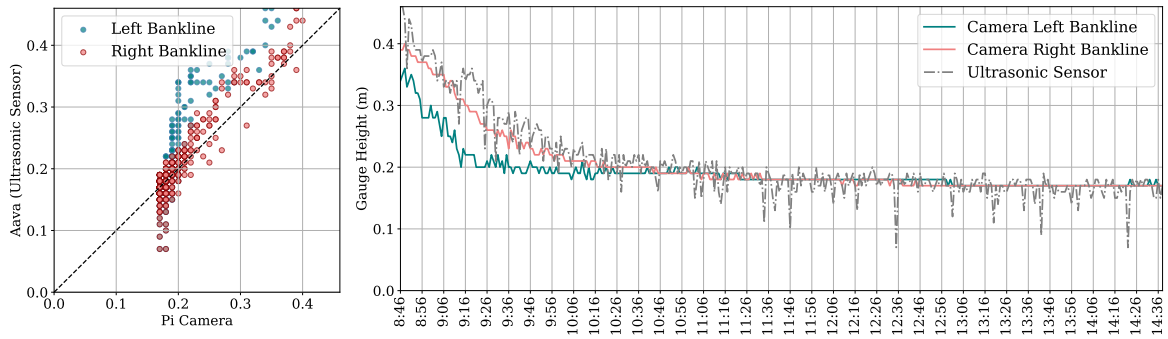
396 The results of the deployments on Nov 10, 2022, and Nov 11, 2022, demonstrate that modifications
397 to the setup have significantly improved the results of the left bank (as shown in Table 3). NSE
398 improved from approximately 0.55 for the first three setup deployments to over 0.80 for the modified
399 deployments. Figure 8 shows the setup performances during all segments of the flood wave. The peaks
400 were captured by the right bankline on both deployment dates, and there was no effect of noisy spikes
401 on either camera readings or ground truth data. However, the right bank images still underestimated
402 the water level during the rainstorms.



(a)



(b)



(c)

Figure 6: Scatter plot and time series plot for estimated water level by the proposed framework and measured by the ultrasonic sensor for setup deployment on (a) Aug 17, 2022 (b) Aug 19, 2022, and (c) Aug 25, 2022.

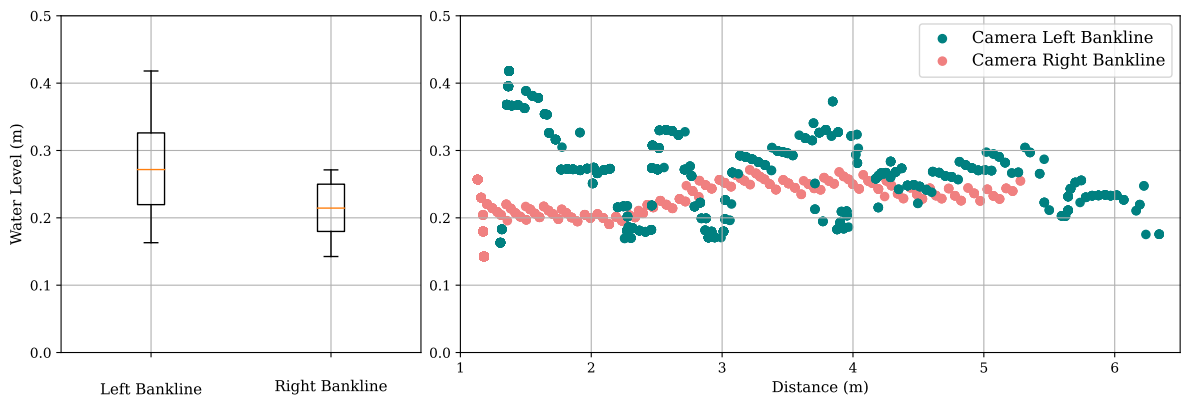


Figure 7: Water level fluctuation along both left and right banks for the flow regime for an image captured at 13:29 on Aug 19, 2022.

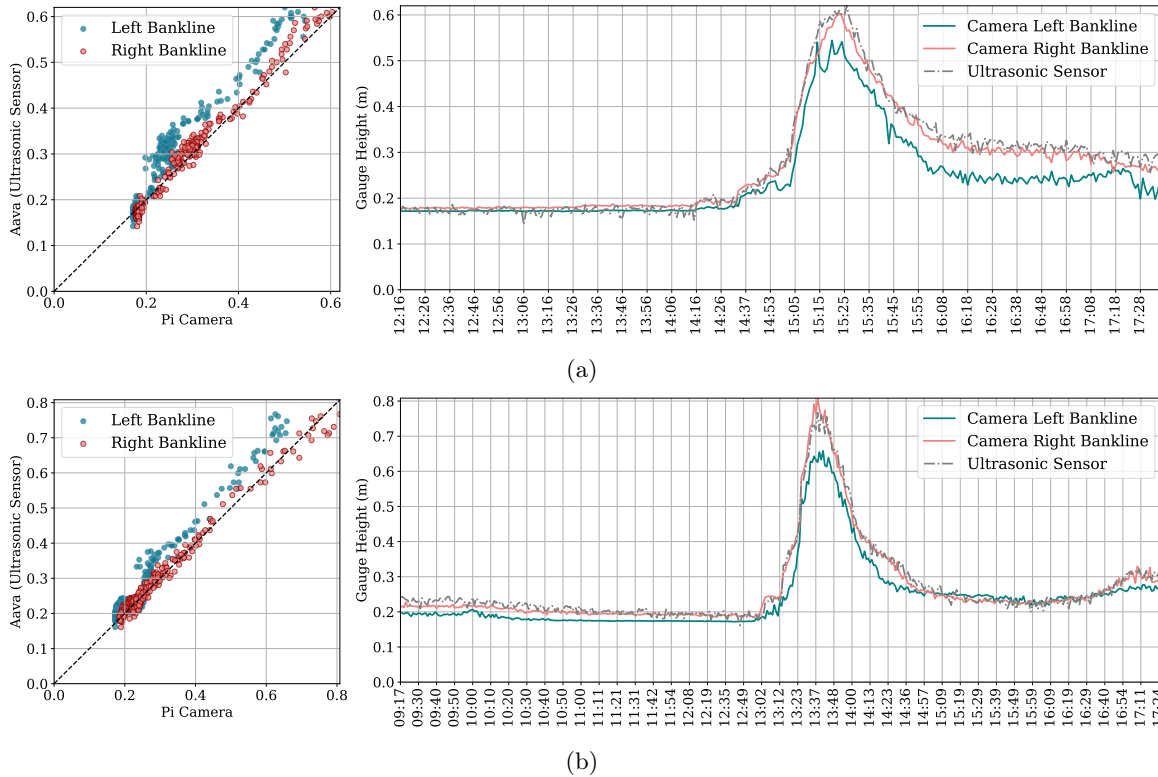


Figure 8: Scatter plot and time series plot for estimated water level by the proposed framework and measured by the ultrasonic sensor for setup deployment on (a) Nov 10, 2022, and (b) Nov 11, 2022.

6 Conclusion

This study introduced Eye of Horus, a vision-based framework for hydrologic monitoring and measuring real-time water-related parameters, e.g., water level, from surveillance images captured during flood events. Time-lapse images and real water level correspondences were collected by Raspberry Pi camera and Arduino HC-SR05 ultrasonic sensor, respectively. Moreover, Computer Vision and Deep Learning techniques were used for semantic segmentation of water surface within the captured images and for reprojecting the 3D point cloud constructed with an iPhone LiDAR scanner, on the (2D) image plane. Eventually, the K-Nearest Neighbor algorithm was used to intersect the projected (2D) point cloud with the water line pixels extracted from the output of the Deep Learning model, to find the real-world 3D coordinates.

A vision-based framework offers a new alternative to current hydrologic data collection and real-time monitoring systems. Hydrological models require geometric information for estimating discharge routing parameters, stage, and flood inundation maps. However, determining bankfull characteristics is a challenge due to natural or anthropogenic down-cutting of streams. Using visual sensing, stream depth, water velocity, and instantaneous streamflow at bankfull stage can be reliably measured.

7 Data Availability Statement

The framework and codes developed and used in this study are available online in the GitHub repository (<https://github.com/smhassanerfani/horus>).

References

Douglas E Alsdorf, Ernesto Rodríguez, and Dennis P Lettenmaier. Measuring surface water from space. *Reviews of Geophysics*, 45(2), 2007.

- 424 Vijay Badrinarayanan, Ankur Handa, and Roberto Cipolla. Segnet: A deep convolutional encoder-
425 decoder architecture for robust semantic pixel-wise labelling. *arXiv preprint arXiv:1505.07293*, 2015.
- 426 G. Bradski. The OpenCV Library. *Dr. Dobb's Journal of Software Tools*, 2000.
- 427 Jieneng Chen, Yongyi Lu, Qihang Yu, Xiangde Luo, Ehsan Adeli, Yan Wang, Le Lu, Alan L Yuille,
428 and Yuyin Zhou. Transunet: Transformers make strong encoders for medical image segmentation.
429 *arXiv preprint arXiv:2102.04306*, 2021.
- 430 Liang-Chieh Chen, George Papandreou, Iasonas Kokkinos, Kevin Murphy, and Alan L Yuille. Deeplab:
431 Semantic image segmentation with deep convolutional nets, atrous convolution, and fully connected
432 crfs. *IEEE Trans. Pattern Anal. Mach. Intell.*, 40(4):834–848, 2017.
- 433 Andrea De Cesare, Shari Cavicchi, Giampaolo Cristadoro, and Marco Lippi. Do humans and deep con-
434 volutional neural networks use visual information similarly for the categorization of natural scenes?
435 *Cognitive Science*, 45(6):e13009, 2021.
- 436 Samuel Dodge and Lina Karam. A study and comparison of human and deep learning recognition
437 performance under visual distortions. In *Int. Conf. Comput. Communication and Networks*, pages
438 1–7. IEEE, 2017.
- 439 Alexey Dosovitskiy, Lucas Beyer, Alexander Kolesnikov, Dirk Weissenborn, Xiaohua Zhai, Thomas
440 Unterthiner, Mostafa Dehghani, Matthias Minderer, Georg Heigold, Sylvain Gelly, et al. An image
441 is worth 16x16 words: Transformers for image recognition at scale. *arXiv preprint arXiv:2010.11929*,
442 2020.
- 443 Melanie Elias, Anette Eltner, Frank Liebold, and Hans-Gerd Maas. Assessing the influence of temper-
444 ature changes on the geometric stability of smartphone-and raspberry pi cameras. *Sensors*, 20(3):
445 643, 2020.
- 446 Anette Eltner and Danilo Schneider. Analysis of different methods for 3d reconstruction of natural
447 surfaces from parallel-axes uav images. *The Photogrammetric Record*, 30(151):279–299, 2015.
- 448 Anette Eltner, Andreas Kaiser, Carlos Castillo, Gilles Rock, Fabian Neugirg, and Antonio Abellán.
449 Image-based surface reconstruction in geomorphometry—merits, limits and developments. *Earth
450 Surface Dynamics*, 4(2):359–389, 2016.
- 451 Anette Eltner, Melanie Elias, Hannes Sardemann, and Diana Spieler. Automatic image-based water
452 stage measurement for long-term observations in ungauged catchments. *Water Resources Research*,
453 54(12):10–362, 2018.
- 454 Anette Eltner, Patrik Olā Bressan, Thales Akiyama, Wesley Nunes Gonçalves, and Jose Marcato Ju-
455 nior. Using deep learning for automatic water stage measurements. *Water Resources Research*, 57
456 (3):e2020WR027608, 2021.
- 457 Seyed Mohammad Hassan Erfani, Zhenyao Wu, Xinyi Wu, Song Wang, and Erfan Goharian. Atlantis:
458 A benchmark for semantic segmentation of waterbody images. *Environmental Modelling & Software*,
459 149:105333, 2022.
- 460 David A Forsyth and Jean Ponce. *Computer vision: a modern approach*. prentice hall professional
461 technical reference, 2002.
- 462 Laurent Froideval, Kevin Pedoja, Franck Garestier, Pierre Moulon, Christophe Conessa, Xavier Pellerin
463 Le Bas, Kalil Traoré, and Laurent Benoit. A low-cost open-source workflow to generate georeferenced
464 3d sfm photogrammetric models of rocky outcrops. *The Photogrammetric Record*, 34(168):365–384,
465 2019.
- 466 Jun Fu, Jing Liu, Haijie Tian, Yong Li, Yongjun Bao, Zhiwei Fang, and Hanqing Lu. Dual attention
467 network for scene segmentation. In *IEEE Conf. Comput. Vis. Pattern Recog.*, pages 3146–3154,
468 2019.
- 469 Asmamaw Gebrehiwot, Leila Hashemi-Beni, Gary Thompson, Parisa Kordjamshidi, and Thomas E
470 Langan. Deep convolutional neural network for flood extent mapping using unmanned aerial vehicles
471 data. *Sensors*, 19(7):1486, 2019.

- 472 Robert Geirhos, Patricia Rubisch, Claudio Michaelis, Matthias Bethge, Felix A Wichmann, and
473 Wieland Brendel. Imagenet-trained cnns are biased towards texture; increasing shape bias improves
474 accuracy and robustness. *arXiv preprint arXiv:1811.12231*, 2018a.
- 475 Robert Geirhos, Carlos RM Temme, Jonas Rauber, Heiko H Schütt, Matthias Bethge, and Felix A
476 Wichmann. Generalisation in humans and deep neural networks. *Adv. Neural Inform. Process. Syst.*,
477 31, 2018b.
- 478 Robert Geirhos, Kristof Meding, and Felix A Wichmann. Beyond accuracy: quantifying trial-by-trial
479 behaviour of cnns and humans by measuring error consistency. *Adv. Neural Inform. Process. Syst.*,
480 33:13890–13902, 2020.
- 481 Troy E Gilmore, François Birgand, and Kenneth W Chapman. Source and magnitude of error in an
482 inexpensive image-based water level measurement system. *Journal of hydrology*, 496:178–186, 2013.
- 483 Christoph Gollob, Tim Ritter, Ralf Kraßnitzer, Andreas Tockner, and Arne Nothdurft. Measurement
484 of forest inventory parameters with Apple iPad pro and integrated LiDAR technology. *Remote
485 Sensing*, 13(16):3129, 2021.
- 486 Michael F Goodchild. Citizens as sensors: the world of volunteered geography. *GeoJournal*, 69(4):
487 211–221, 2007.
- 488 Kaiming He, Xiangyu Zhang, Shaoqing Ren, and Jian Sun. Deep residual learning for image recogni-
489 tion. In *IEEE Conf. Comput. Vis. Pattern Recog.*, pages 770–778, 2016.
- 490 Jeff Howe. *Crowdsourcing: How the power of the crowd is driving the future of business*. Random
491 House, 2008.
- 492 Zilong Huang, Xinggang Wang, Lichao Huang, Chang Huang, Yunchao Wei, and Wenyu Liu. Ccnet:
493 Criss-cross attention for semantic segmentation. In *Int. Conf. Comput. Vis.*, pages 603–612, 2019.
- 494 J Kim, Y Han, and H Hahn. Embedded implementation of image-based water-level measurement
495 system. *IET computer vision*, 5(2):125–133, 2011.
- 496 Tyler V King, Bethany T Neilson, and Mitchell T Rasmussen. Estimating discharge in low-order rivers
497 with high-resolution aerial imagery. *Water Resources Research*, 54(2):863–878, 2018.
- 498 Wouter JM Knoben, Jim E Freer, and Ross A Woods. Inherent benchmark or not? comparing nash-
499 sutcliffe and kling-gupta efficiency scores. *Hydrology and Earth System Sciences*, 23(10):4323–4331,
500 2019.
- 501 Peter Krause, DP Boyle, and Frank Bäse. Comparison of different efficiency criteria for hydrological
502 model assessment. *Advances in Geosciences*, 5:89–97, 2005.
- 503 LAAN LABS. 3D Scanner App – LiDAR Scanner for iPad Pro & iPhone Pro. Available online:
504 <https://3dscannerapp.com/>, 2022. Accessed on Sep 16, 2022.
- 505 Xia Li, Zhisheng Zhong, Jianlong Wu, Yibo Yang, Zhouchen Lin, and Hong Liu. Expectation-
506 maximization attention networks for semantic segmentation. In *Int. Conf. Comput. Vis.*, pages
507 9167–9176, 2019.
- 508 Zhenlong Li, Cuizhen Wang, Christopher T Emrich, and Diansheng Guo. A novel approach to leverag-
509 ing social media for rapid flood mapping: a case study of the 2015 south carolina floods. *Cartography
510 and Geographic Information Science*, 45(2):97–110, 2018.
- 511 Guosheng Lin, Anton Milan, Chunhua Shen, and Ian Reid. Refinenet: Multi-path refinement networks
512 for high-resolution semantic segmentation. In *IEEE Conf. Comput. Vis. Pattern Recog.*, pages 1925–
513 1934, 2017.
- 514 Peirong Lin, Ming Pan, George H Allen, Renato Prata de Frasson, Zhenzhong Zeng, Dai Yamazaki,
515 and Eric F Wood. Global estimates of reach-level bankfull river width leveraging big data geospatial
516 analysis. *Geophysical Research Letters*, 47(7):e2019GL086405, 2020.

- 517 Ze Liu, Yutong Lin, Yue Cao, Han Hu, Yixuan Wei, Zheng Zhang, Stephen Lin, and Baining Guo.
518 Swin transformer: Hierarchical vision transformer using shifted windows. In *Int. Conf. Comput.*
519 *Vis.*, pages 10012–10022, 2021.
- 520 Shi-Wei Lo, Jyh-Horng Wu, Fang-Pang Lin, and Ching-Han Hsu. Visual sensing for urban flood
521 monitoring. *Sensors*, 15(8):20006–20029, 2015.
- 522 Jonathan Long, Evan Shelhamer, and Trevor Darrell. Fully convolutional networks for semantic seg-
523 mentation. In *IEEE Conf. Comput. Vis. Pattern Recog.*, pages 3431–3440, 2015.
- 524 Ilya Loshchilov and Frank Hutter. Decoupled weight decay regularization. *arXiv preprint*
525 *arXiv:1711.05101*, 2017.
- 526 Gregor Luetzenburg, Aart Kroon, and Anders A Bjørk. Evaluation of the apple iphone 12 pro lidar
527 for an application in geosciences. *Scientific reports*, 11(1):1–9, 2021.
- 528 Eric Marchand, Hideaki Uchiyama, and Fabien Spindler. Pose estimation for augmented reality: a
529 hands-on survey. *IEEE Trans. Pattern Anal. Mach. Intell.*, 22(12):2633–2651, 2015.
- 530 Shervin Minaee, Yuri Y Boykov, Fatih Porikli, Antonio J Plaza, Nasser Kehtarnavaz, and Demetri
531 Terzopoulos. Image segmentation using deep learning: A survey. *IEEE Trans. Pattern Anal. Mach.*
532 *Intell.*, 2021.
- 533 Martin Mokroš, Tomáš Mikita, Arunima Singh, Julián Tomaščík, Juliána Chudá, Piotr Wężyk, Karel
534 Kuželka, Peter Surový, Martin Klimánek, Karolina Zięba-Kulawik, et al. Novel low-cost mobile
535 mapping systems for forest inventories as terrestrial laser scanning alternatives. *International Journal*
536 *of Applied Earth Observation and Geoinformation*, 104:102512, 2021.
- 537 Mohamed M Morsy, Jonathan L Goodall, Fadi M Shatnawi, and Michael E Meadows. Distributed
538 stormwater controls for flood mitigation within urbanized watersheds: case study of rocky branch
539 watershed in columbia, south carolina. *Journal of Hydrologic Engineering*, 21(11):05016025, 2016.
- 540 Matthew Moy de Vitry, Simon Kramer, Jan Dirk Wegner, and João P Leitão. Scalable flood level
541 trend monitoring with surveillance cameras using a deep convolutional neural network. *Hydrology*
542 *and Earth System Sciences*, 23(11):4621–4634, 2019.
- 543 Muhammad Muzammal Naseer, Kanchana Ranasinghe, Salman H Khan, Munawar Hayat, Fahad
544 Shahbaz Khan, and Ming-Hsuan Yang. Intriguing properties of vision transformers. *Adv. Neural*
545 *Inform. Process. Syst.*, 34:23296–23308, 2021.
- 546 Hyeonwoo Noh, Seunghoon Hong, and Bohyung Han. Learning deconvolution network for semantic
547 segmentation. In *Int. Conf. Comput. Vis.*, pages 1520–1528, 2015.
- 548 RJ Pally and S Samadi. Application of image processing and convolutional neural networks for flood
549 image classification and semantic segmentation. *Environmental Modelling & Software*, 148:105285,
550 2022.
- 551 George Panteras and Guido Cervone. Enhancing the temporal resolution of satellite-based flood ex-
552 tent generation using crowdsourced data for disaster monitoring. *International Journal of Remote*
553 *Sensing*, 39(5):1459–1474, 2018.
- 554 E Schnebele, G Cervone, and N Waters. Road assessment after flood events using non-authoritative
555 data. *Natural Hazards and Earth System Sciences*, 14(4):1007, 2014.
- 556 Elyas Asadi Shamsabadi, Chang Xu, and Daniel Dias-da Costa. Robust crack detection in masonry
557 structures with transformers. *Measurement*, 200:111590, 2022.
- 558 Corinne Smith, Joud Satme, Jacob Martin, Austin R.J. Downey, Nikolaos Vitzilaios, and Jasim Imran.
559 UAV rapidly-deployable stage sensor with electro-permanent magnet docking mechanism for flood
560 monitoring in undersampled watersheds. *HardwareX*, 12:e00325, oct 2022. doi: 10.1016/j.ohx.2022.
561 e00325.
- 562 Stefano Tavani, Andrea Billi, Amerigo Corradetti, Marco Mercuri, Alessandro Bosman, Marco Cuf-
563 faro, Thomas Seers, and Eugenio Carminati. Smartphone assisted fieldwork: Towards the digital

564 transition of geoscience fieldwork using lidar-equipped iphones. *Earth-Science Reviews*, 227:103969,
565 2022.

566 Ryota Tsubaki, Ichiro Fujita, and Shiho Tsutsumi. Measurement of the flood discharge of a small-sized
567 river using an existing digital video recording system. *Journal of Hydro-environment Research*, 5
568 (4):313–321, 2011.

569 D Phil Turnipseed and Vernon B Sauer. Discharge measurements at gaging stations. Technical report,
570 US Geological Survey, 2010.

571 Ashish Vaswani, Noam Shazeer, Niki Parmar, Jakob Uszkoreit, Llion Jones, Aidan N Gomez, Łukasz
572 Kaiser, and Illia Polosukhin. Attention is all you need. *Adv. Neural Inform. Process. Syst.*, 30, 2017.

573 Maximilian Vogt, Adrian Rips, and Claus Emmelmann. Comparison of ipad pro®’s lidar and
574 truedepth capabilities with an industrial 3d scanning solution. *Technologies*, 9(2):25, 2021.

575 Matthew J Westoby, James Brasington, Niel F Glasser, Michael J Hambrey, and Jennifer M Reynolds.
576 ‘structure-from-motion’photogrammetry: A low-cost, effective tool for geoscience applications. *Ge-*
577 *omorphology*, 179:300–314, 2012.

578 Enze Xie, Wenhai Wang, Zhiding Yu, Anima Anandkumar, Jose M Alvarez, and Ping Luo. Segformer:
579 Simple and efficient design for semantic segmentation with transformers. *Adv. Neural Inform. Pro-*
580 *cess. Syst.*, 34:12077–12090, 2021.

581 Yuhui Yuan and Jingdong Wang. Ocnet: Object context network for scene parsing. *arXiv preprint*
582 *arXiv:1809.00916*, 2018.

583 Yuhui Yuan, Xilin Chen, and Jingdong Wang. Object-contextual representations for semantic segmen-
584 tation. In *Eur. Conf. Comput. Vis.*, pages 173–190. Springer, 2020.

585 Zhen Zhang, Yang Zhou, Haiyun Liu, and Hongmin Gao. In-situ water level measurement using
586 nir-imaging video camera. *Flow Measurement and Instrumentation*, 67:95–106, 2019.

587 Hengshuang Zhao, Jianping Shi, Xiaojuan Qi, Xiaogang Wang, and Jiaya Jia. Pyramid scene parsing
588 network. In *Proceedings of the IEEE conference on computer vision and pattern recognition*, pages
589 2881–2890, 2017.

590 Yufeng Zheng, Jun Huang, Tianwen Chen, Yang Ou, and Wu Zhou. Processing global and local features
591 in convolutional neural network (cnm) and primate visual systems. In *Mobile Multimedia/Image*
592 *Processing, Security, and Applications 2018*, volume 10668, pages 44–51. SPIE, 2018.

593 Zhen Zhu, Mengde Xu, Song Bai, Tengting Huang, and Xiang Bai. Asymmetric non-local neural
594 networks for semantic segmentation. In *Int. Conf. Comput. Vis.*, pages 593–602, 2019.